Journal of Asian Earth Sciences 249 (2023) 105625

Contents lists available at ScienceDirect

Journal of Asian Earth Sciences

journal homepage: www.elsevier.com/locate/jseaes

Quantifying the relative contribution and evolution of pore types to shale reservoir space: Constraints from over-mature marine shale in the Sichuan Basin, SW China

Shasha Hui [a,b], Xiongqi Pang [a,b,*], Zhuoheng Chen [c], Tao Hu [a,b], Kanyuan Shi [a,b], Guidong Di [d], Min Li [a,b], Shuxing Mei [a,b], Maowen Li [e]

[a] State Key Laboratory of Petroleum Resources and Prospecting, China University of Petroleum (Beijing), Beijing 102249, China
[b] College of Geosciences, China University of Petroleum (Beijing), Beijing 102249, China
[c] Geological Survey of Canada, Natural Resources Canada, Calgary T2L 2A7, Canada
[d] Research Institute of Exploration and Development, Southwest Oil & Gas Field Company, Chengdu 610041, China
[e] China State Key Laboratory of Shale Oil and Shale Gas Resources and Effective Development, Sinopec Petroleum Exploration and Production Research Institute, Beijing 100083, China

ARTICLE INFO

Keywords:
Over-mature shale
Pore types
Quantitative characterization
Relative contribution
Lower Silurian Longmaxi Formation

ABSTRACT

Pore types significantly affect the pore properties of shale reservoirs, but their contribution to shale pore space in over-mature marine shale remains controversial because organic and inorganic pores fail to be quantitatively characterized. In this study, mercury intrusion porosimetry, low-temperature N_2 and CO_2 adsorption, and image analysis were conducted on over-mature marine shale in the Lower Silurian Longmaxi Formation to quantify the contribution of pore types to pore volume (PV) and surface area (SA). The full-scale pore size distribution of over-mature shale indicates that mesopores account for the largest PV, while macropores are developed in organic matter (OM)-poor shale. By analyzing the influence of multiple factors and heterogeneity of different pore types, OM pores, pyrite framboid pores, clay mineral pores, and dissolution pores are identified as dominant types in OM-poor/moderate/rich shale. The PV and SA of these four pore types are quantitatively characterized by extracting parameters of shale components and pores using image analysis. In OM-poor shale, clay mineral pores contribute the most to the PV and SA, followed by OM pores and dissolution pores, and finally pyrite framboid pores. In OM-rich/moderate shale, the contribution of OM pores to the PV and SA is dominant and increases with the increasing total organic carbon content. The evolution of pore types throughout the maturation sequence is revealed based on previous studies. Especially at the over-mature stage, clay mineral pores contribute the most to pore space in OM-poor shale, while OM pores make a major contribution to pore space in OM-rich/moderate shale.

1. Introduction

In recent years, China's oil and gas industry has focused on exploring deep shale oil and gas resources because of the conventional hydrocarbon resource shortage (Wang et al., 2022a). Following commercial exploitation in the United States (US), the discovery of deep shale gas in the Sichuan Basin has fueled further enthusiasm for shale reservoir exploration (Chen et al., 2020; Li et al., 2021a). Because of the influence of diagenesis and a process involving hydrocarbon generation and expulsion (Jarvie et al., 2007; Mastalerz et al., 2013; Peng et al., 2020a, b), shale reservoirs have more pore types than conventional reservoirs (Slatt and O'Brien, 2011; Loucks et al., 2012). Various pore types lead to great differences in shale physical properties, pore structure, pore size distribution (PSD), heterogeneity, even fluid mobility and gas occurrence (Nelson, 2009; Chen et al., 2016, 2021; Tian et al., 2020; Sun et al., 2021; Gao et al., 2021). It is, therefore, essential to clarify the contribution of pore types to pore space.

In the past two decades, pore types (Slatt and O'Brien, 2011; Loucks et al., 2009, 2012), pore structures (Katsube and Issler, 1993; Daniel and Marc, 2009; Tian et al., 2013; Cao et al., 2015; Xu et al., 2020; Wu et al., 2022; Zhao et al., 2022; Shi et al., 2023), fractal features (Yang et al., 2014; Tang et al., 2015, 2016; Wang et al., 2016; Zhong et al., 2021),

* Corresponding author at: State Key Laboratory of Petroleum Resources and Prospecting, China University of Petroleum (Beijing), Beijing 102249, China.
E-mail address: pangxq@cup.edu.cn (X. Pang).

https://doi.org/10.1016/j.jseaes.2023.105625
Received 8 September 2022; Received in revised form 8 March 2023; Accepted 10 March 2023
Available online 15 March 2023

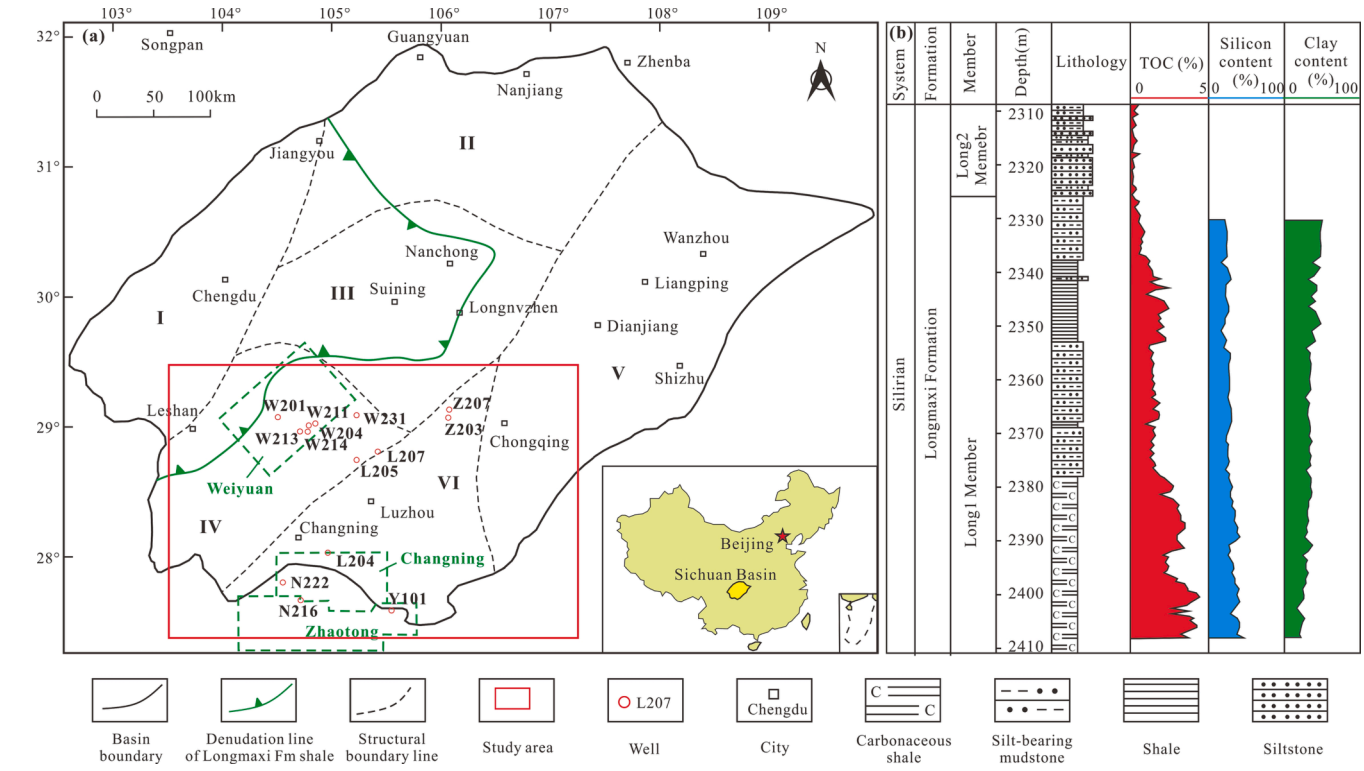

Fig. 1. Comprehensive map of structural and stratigraphic characteristics of the Sichuan Basin. (a) Structural distribution. I – Low and Steep Belt in western Sichuan; II – Low and Flat Fold Belt in northern Sichuan; III – Gentle belt in central Sichuan; IV – Low and Steep Belt in southwestern Sichuan; V – High and Steep Fold Belt in eastern Sichuan; VI – Low and Steep Belt in southern Sichuan. (b) Stratigraphic column (modified from Guo et al., 2020).

Table 1
TOC, EqRo, and mineral components in the Longmaxi shale.

Well	Sample ID	Depth (m)	TOC (%)	EqRo (%)	Mineral content (%)						Relative content of clay minerals (%)			Reflectivity measuring object
					Quartz	Feldspar	Calcite	Dolomite	Pyrite	Clay	Illite	Chlorite	I/S	
L204	L1	3327.6	4.43	2.82	41.5	5.9	6.2	4.1	6.1	36.2	74	10	16	SB
	L2	3836.0	4.1	/	49.6	4.3	8	10.7	9.3	18.1	78	5	17	/
	L3	3991.2	3.18	2.79	30.8	10.1	3.2	15.6	3.4	36.9	72	13	15	SB
L205	L4	3994.1	2.99	/	/	/	/	/	/	/	/	/	/	/
	L5	4012.5	2.47	2.57	47	7	4.3	6.3	2.4	33	66	10	24	SB
L207	L6	3410.0	3.62	2.93	29.6	6.8	14.4	14.1	6.1	29	70	11	19	SB
	L7	3912.0	2.17	2.95	31.2	6.5	6.6	6.9	2.3	46.5	71	9	20	SB
N216	N1	2300.9	1.1	3.17	35.6	20.8	7	7.4	1.4	27.8	66	19	15	SB
N222	N2	4307.4	3.89	/	35.3	7.9	4.6	3.5	4.7	44	66	16	18	/
W204	W1	3354.8	4.24	/	48.9	2.7	6.7	13.8	1.8	26.1	73	9	18	/
W211	W2	3511.1	0.44	2.23	40.1	6	0.8	/	2.8	50.3	65	25	10	Graptolite
W213	W3	3717.8	2.51	2.97	30.7	3.2	21.4	12.7	3.2	28.8	69	11	20	SB
W214	W4	3525.0	1.32	/	37.4	6.6	3.9	5.3	3	43.8	63	20	17	/
W231	W5	3732.9	3.94	2.86	33.8	9.5	2.5	7.8	5.4	41	70	10	20	SB
Y101	Y1	4073.6	0.42	/	/	/	/	/	/	/	/	/	/	/
	Y2	4138.7	4.67	/	45.2	5.1	1.7	3	6.6	38.4	70	9	21	/
	Y3	4088.2	2.58	/	30.6	5.8	4.3	15.9	2.4	41	75	13	12	/
Z203	Z1	4060.0	1.95	2.81	32.8	5.4	1.6	4.4	4.3	51.5	63	16	21	SB
Z207	Z2	4353.8	0.46	2.68	44.9	4.7	0.9	2.4	2.5	44.6	66	14	20	Graptolite
	Z3	4384.5	3.23	2.80	64.9	3.7	2	3.6	1.9	23.9	76	9	15	SB

influencing factors (Ross and Marc Bustin, 2009; Furmann et al., 2014; Li et al., 2021a), and pore evolution (Pommer and Milliken, 2015; Mathia et al., 2016; Ko et al., 2018; Xu et al., 2021a,b; Cao et al., 2022) have been extensively studied using scanning electron microscopy (SEM), mercury intrusion porosimetry (MIP), low-temperature gas adsorption (LTGA), computed tomography (CT) scanning, and nuclear magnetic resonance (NMR) (Li et al., 2015; Nie et al., 2021; Chen et al., 2021). SEM is the most direct and effective qualitative method for observing pore types. Shale pores are generally divided into mineral-related pores (including interparticle and intraparticle pores) and organic-matter (OM) pores (Loucks et al., 2012). The former constitutes a flow network with natural fractures, providing permeability channels for gas flow within shale reservoirs (Slatt and O'Brien, 2011; Zhao et al., 2017; Loucks et al., 2012). While the latter is produced by OM decomposition during the hydrocarbon generation process (Jarvie et al., 2007). The MIP, LTGA, and NMR can quantitatively determine the porosity,

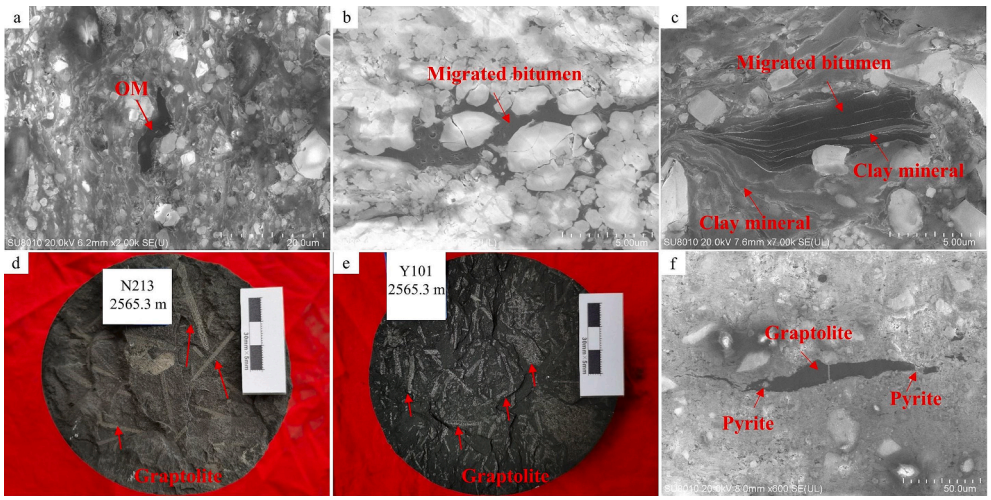

Fig. 2. FE-SEM images and core observations showing the characteristics of OM. (a) Dispersive OM, L3. (b) Migrated bitumen, void-filling shape, Z1. (c) Migrated bitumen, mixed with clay minerals, W5. (d) Graptolite, large-scale and intact morphology, N213. (e) Graptolite, fragmented morphology, Y101. (f) Graptolite, filled by pyrite, Z2.

PSD, pore volume (PV), and surface area (SA) of the bulk shale sample, but fail to distinguish pore parameters of different pore types. Image analysis can effectively utilize abundant high-resolution SEM images to determine the size, geometry, SA, and other properties of different types of pores, OM, and minerals (Chen et al., 2016; Liu et al., 2019; Chandra et al., 2020; Peng et al., 2020a). However, image analysis is highly scale- and location-dependent, and it may not be suitable for pores smaller than 5 nm (Arif et al., 2021; Chandra and Vishal, 2021). Hence, it is necessary to investigate the contribution of pore types to shale pore space using multi-scale qualitative and quantitative methods.

Great progress has been made in exploring the pore characteristics of shale reservoirs, while the contribution of different pore types to shale pore space remains controversial. OM pores were considered to account for 31%–62% of the total porosity in the Longmaxi shale (Tian et al., 2013). Mathia et al. (2016) proposed that mineral-related pores mainly contributed to porosity before the gas window stage in the Posidonia marine shale. Conversely, Cao et al. (2022) believed that mineral-related pores contributed more to porosity at a low maturity, while OM pores did so at gas window maturity. More and more attention has been paid to the contribution of pore types to shale PV and SA with the deepening of research. For the lacustrine shale of the Triassic Yanchang Formation in the Ordos Basin, the contribution of OM pores to the PV reached 1.9%–88.73% and increased with the increasing total organic carbon (TOC) content (Han et al., 2019). For the lacustrine shale of the Jurassic Ziliujing Formation in the Sichuan Basin, Gao et al. (2021) considered that clay mineral pores contributed the most to the PV, followed by pores developed in quartz and feldspar, and finally OM pores. In OM-rich marine shale, Li et al. (2022b) found that >90% of pores were OM pores, contributing the most to the PV and SA. Nevertheless, the influence of mineral-related pores on the porosity, PV, and SA of shale with low TOC content or low maturity cannot be ignored (Ross and Marc Bustin, 2009; Cao et al., 2022). Sedimentary environment, maturity, and TOC content may affect the contribution of pore types to shale pore space.

The Longmaxi shale has been extensively studied (Wang et al., 2022b). Although the pore structure and relative proportion of different pore sizes (micropores, mesopores, and macropores) in the Longmaxi shale have been revealed (Guo et al., 2020; Jiang et al., 2016, 2020; Lyu et al., 2020; Wang et al., 2020; Li et al., 2022a), the contribution of different mineral-related pores (e.g., dissolution pores, pyrite framboid pores, and clay mineral pores) and OM pores to pore space in over-mature marine Longmaxi shale has not been quantified. In this study, qualitative (geochemical analysis, SEM) and quantitative (MIP, LTGA, and image analysis) methods were integrated to investigate pore structure, physical properties, and influencing factors of different pore types in over-mature marine shale. Furthermore, different pore types were systematically extracted and quantitatively characterized using image analysis. The contribution of different pore types to the PV and SA was calculated and compared. Finally, based on previous studies, the contribution evolution of different pore types in the Longmaxi shale is summarized.

2 Geological setting

The Sichuan Basin, which includes six tectonic units, is a large-scale petroliferous basin located in southwestern China (Fig. 1a). Six formations of marine, transitional, and continental shale are widely developed in the Sichuan Basin. The southern part of the Sichuan Basin was selected for our study. It covers an area of 8.8×10^4 km^2, including several major shale gas exploration demonstration areas in China, such as Changning, Weiyuan, and Zhaotong (Dai et al., 2014; Fig. 1a). The Longmaxi Formation developed as a deep-water shelf facies, forming in a limited hydrostatic environment. A set of thick black shale was deposited (50–600 m), which is characterized as OM-rich (TOC > 2%), high maturity (equivalent vitrinite reflectance (EqRo) > 2%), and high brittleness (Zhao et al., 2016; Ma and Xie, 2018). The Longmaxi shale is considered the most promising target for shale gas exploration in the Sichuan Basin (Ma et al., 2018). The Longmaxi Formation can be divided into the first member (Long1) and the second member (Long2) from bottom to top. Long1 Member is mainly composed of dark-gray shale, carbonaceous shale, and graptolitic shale, while Long2 Member mainly consists of calcareous silty shale and siltstone. The grain size becomes coarser and the OM abundance decreases as the member progresses from Long1 to Long2 (Dai et al., 2014; Li et al., 2021b; Fig. 1b).

3 Materials and Methods

3.1 Sample selection

A total of 20 core samples were gathered from the Longmaxi Formation in the southern part of the Sichuan Basin (Fig. 1a). The locations of these samples are distributed as widely as possible throughout the study area. It is widely recognized that the shale in the Longmaxi Formation is high-mature and over-mature. The burial depth of 20 core samples ranges from 2300 to 4385 m. Firstly, the TOC content measurement, equivalent vitrinite reflectance analysis, X-ray diffraction

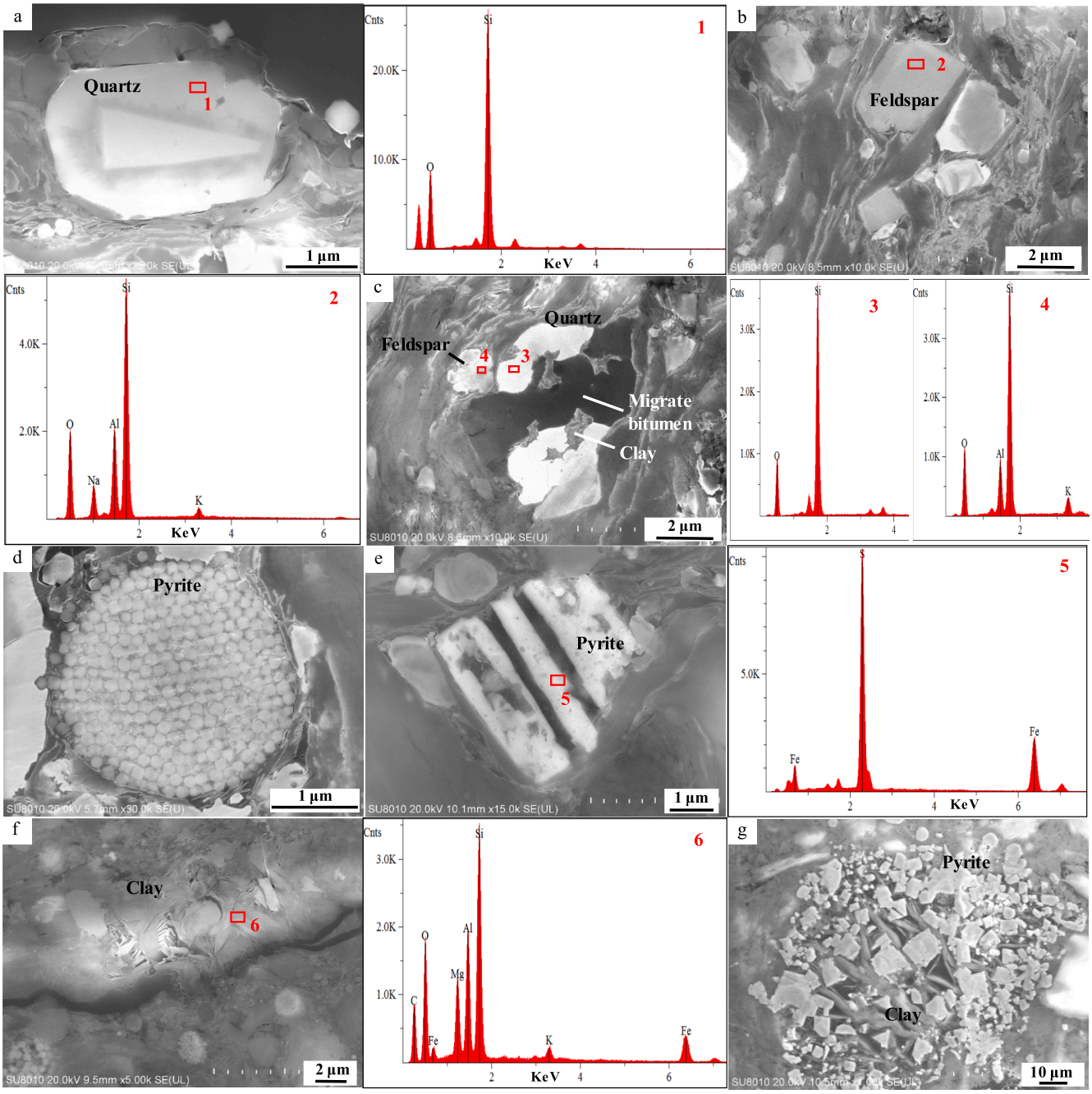

Fig. 3. FE-SEM images with EDS showing different minerals in Longmaxi shale in the study area. (a) Quartz, euhedral-granular, L6. (b) Feldspar, euhedral-granular, L3. (c) Authigenic quartz cement, with clay mineral and migrated bitumen, L3. (d) Pyrite framboid, Z1. (e) Dissolution euhedral pyrite, OM filling, L6. (f) Kaolinite, sheet-like, L1. (g) Clay mineral mixed with pyrite and OM, L5.

(XRD), field emission scanning electron microscopy (FE-SEM), and energy dispersive spectrum (EDS) were adopted to determine the geochemical characteristics and shale pore types. Then, a sequence of shale (7 samples) with different TOC contents and maturities was screened for MIP, LTGA (N_2 and CO_2), and image analysis to analyze shale pore structures.

3.2 Methods

3.2.1 Geochemical and mineral analysis

In this study, 20 sets of TOC contents, 12 sets of Ro values, and 18 sets of mineral analysis results are obtained and listed in Table 1 below. A LECO CS-400 analyzer was employed to analyze TOC contents. The XRD analysis was conducted using the Japanese Rigaku TTR multifunctional X-ray diffractometer. According to the Chinese standard SY/T 5163–2018, each sample was crushed (<40 μm) and then scanned from 2° to 80° at a speed of 0.02°/min at 45 kV and 200 mA. Due to the lack of vitrinite in the marine shale of the Longmaxi Formation, the reflectances of solid bitumen (BRo) and graptolite (GRo) were measured via oil immersion at 546 nm wavelength under a Leica DM4500P polarizing microscope using a reflected-light 50 × objective lens equipped with an MPS200 photometer. According to the formulas proposed by Schoenherr et al. (2007) and Petersen et al. (2013), the BRo and GRo were converted into the EqRo, as shown below:

$$EqRo = BRo \times 0.9528 + 0.2328 (1)$$

$$EqRo = GRo \times 0.73 + 0.16 (2)$$

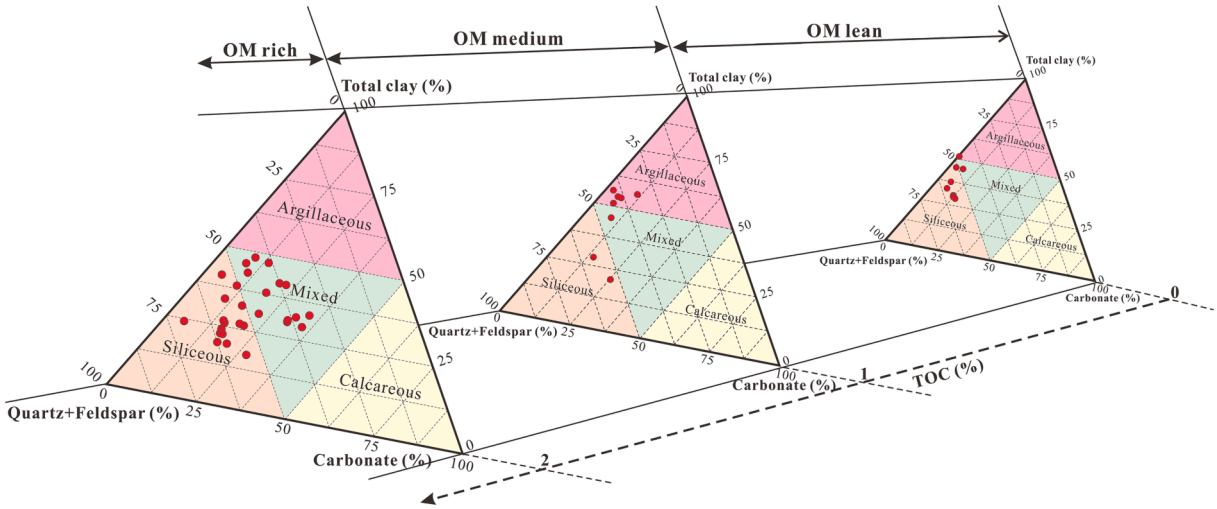

Fig. 4. Triangular diagram of mineral composition of different TOC contents in the Longmaxi shale (). adapted from Lazar et al., 2015

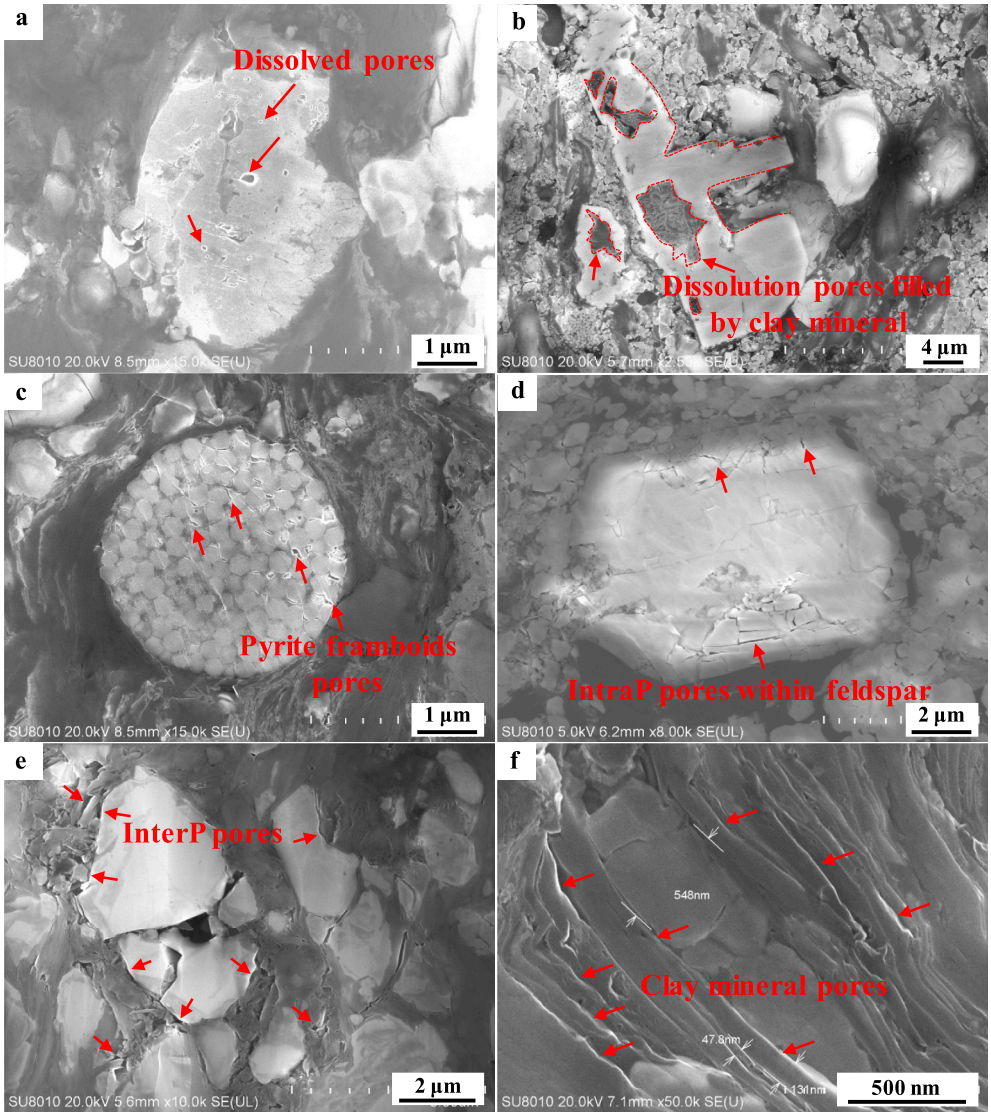

Fig. 5. FE-SEM images showing intraP pores and interP pores. (a) Independent and round dissolution pores, L3. (b) Large-scale dissolution pores, Z1. (c) IntraP pores within pyrite framboids, Z1. (d) Microcracks within brittle minerals, Z3. (e) InterP pores between quartz and clay minerals, W2. (f) InterP pores between clay flakes, W3.

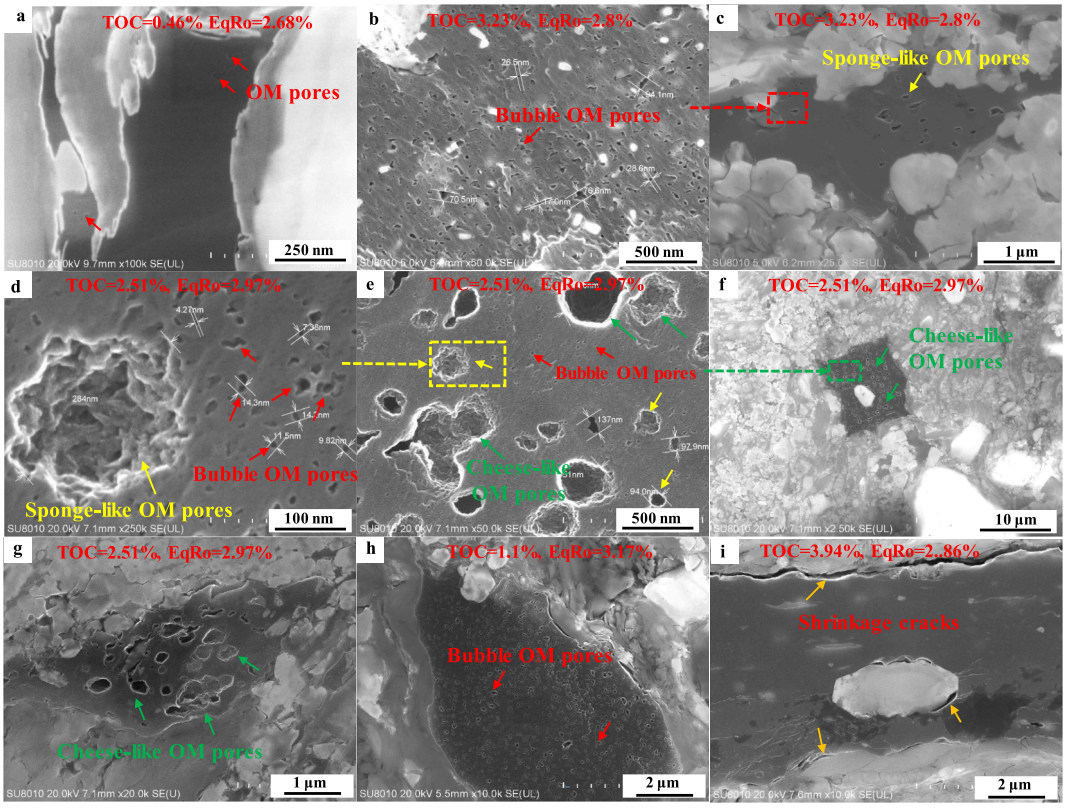

Fig. 6. FE-SEM images showing the characteristics of bubble, sponge-like, and cheese-like OM pores, as well as shrinkage cracks (red, yellow, green, and orange arrows, respectively), with the increasing maturity. (a) Rare OM pore in low TOC shale, Z2. (b) Uniformly distributed bubble OM pores revealed by the local magnification of (c) at extremely high resolution, Z3. (c) Sporadic distribution of sponge-like OM pores in high TOC samples at a lower magnification, Z3. (d) Independent and dense bubble OM pores revealed by the local magnification of (e) at an extremely high resolution, W3. (e) Independent and round sponge-like OM pores revealed by the local magnification of (f), W3. (f) Connected and large-scale cheese-like OM pores, W3. (g) Developed large-scale cheese-like OM pores, W3. (h) Developed bubble OM pores in over-mature shale, N1. (i) Shrinkage cracks, W5. (For interpretation of the references to colour in this figure legend, the reader is referred to the web version of this article.)

Table 2
Pore structure parameters of the Longmaxi shale.

Sample ID	MIP			Low-temperature N_2 adsorption		Low-temperature CO_2 adsorption	
	Porosity (%)	Average pore diameter (nm)	Pore volume (cm^3/g)	BET surface area (m^2/g)	BJH pore volume (cm^3/g)	DFT surface area (m^2/g)	DFT pore volume (cm^3/g)
L1	7.02	12	0.027	17.95	0.012	17.75	0.005
L5	5.14	356	0.020	17.34	0.009	15.54	0.005
L6	3.98	12	0.015	24.83	0.009	20.92	0.006
N1	2.59	10	0.010	9.45	0.006	9.18	0.003
W3	6.04	12	0.023	23.35	0.015	17.21	0.005
Z2	4.81	138	0.018	9.39	0.006	9.20	0.003
Z3	4.13	12	0.016	20.17	0.009	19.10	0.006

3.2.2 FE-SEM observations

Firstly, the shale samples were sectioned vertically and polished by an argon ion beam to obtain a smooth surface for improved image quality. Then, the shale pore structures and mineral types were visualized and semi-quantitatively analyzed by the FEI Quanta 200F FE-SEM system equipped with an EDS. As the magnification of the FE-SEM system could reach 25 k to 200 k, pores ranging from several nanometers to tens of microns could be observed under the microscope. The FE-SEM and EDS enabled the internal structure and composition distribution of shale to be identified, such as the relationship between minerals, OM, and pores. In addition, informative data such as pore type, location, size, and morphology were obtained.

3.2.3 Mercury intrusion porosimetry (MIP)

Firstly, a $1 \times 1 \times 1$ cm^3 cube of shale was dried in an oven for 48 h at 105℃ and then cooled to room temperature. Pore characterization and porosity measurements were conducted using a Micromeritics Autopore IV 9505 instrument at an experimental temperature of 21.5 °C and a humidity of 40%. Non-wetting mercury was injected into shale pores under increasing pressure, which could overcome the capillary force of shale pores and preferentially enter larger pores. Then, according to the Washburn equation, the pore radii corresponding to different mercury injection pressures were obtained, and the amount of injected mercury under different pressures was the PV corresponding to the pore size (Washburn, 1921). The MIP's maximum pressure was 200 MPa, and the measurement aperture ranged from 200 μm to 8 nm. Excessive experimental pressure (>200 MPa) would not only damage the experimental instrument but also cause fractures in shale samples, producing larger porosity measurement results (Jiang et al., 2016). Moreover, the conformance effect could be a source of error when calculating

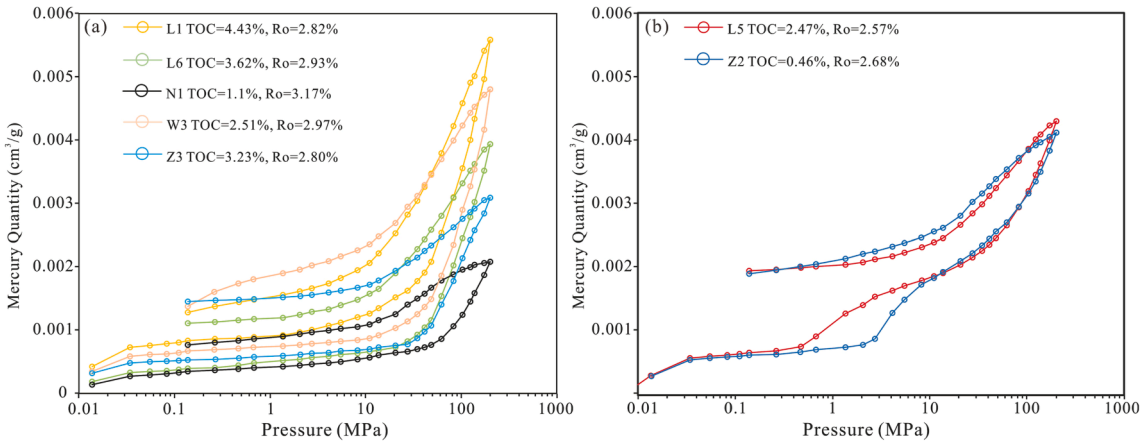

Fig. 7. Characteristics of MIP curves in the Longmaxi shale.

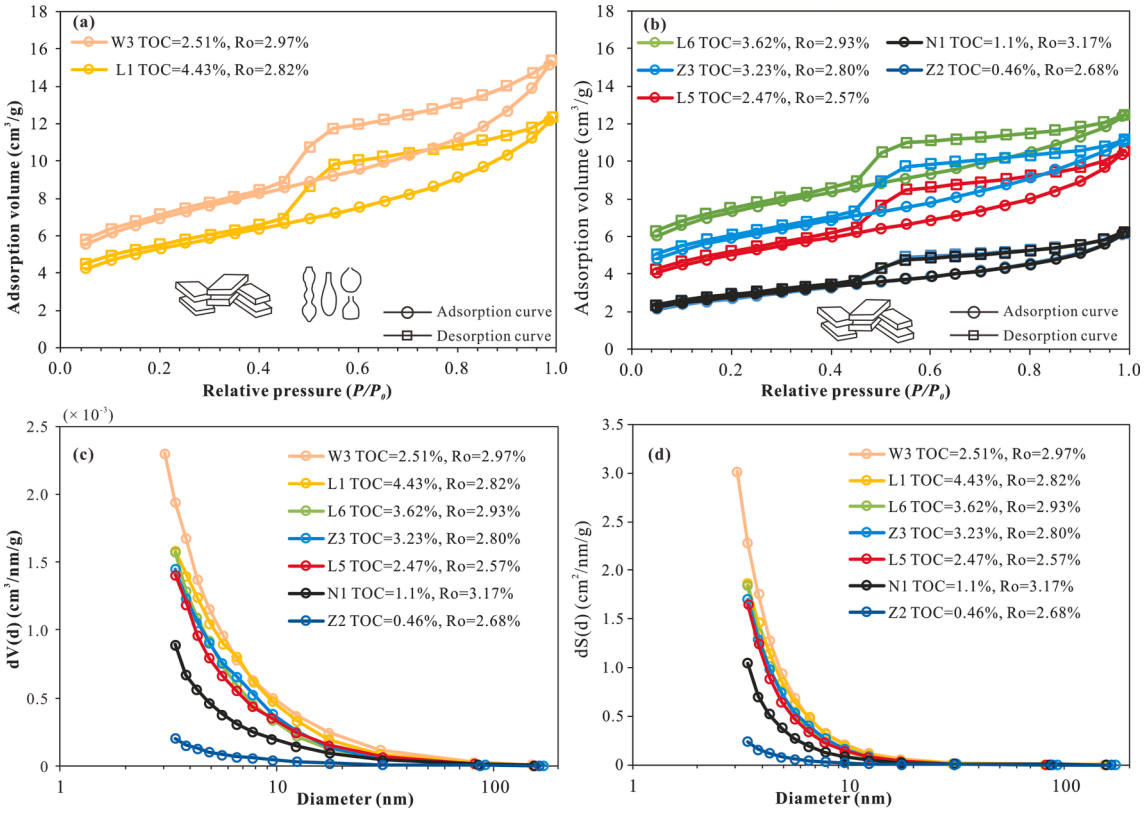

Fig. 8. The characteristics of N_2 adsorption isotherms and PSD of the Longmaxi shale in the study area obtained by LTN_2A.

petrophysical properties from MIP on shale samples (Comisky et al., 2011). Conformance increased on crushed samples with smaller particle sizes due to mercury entering the voids between grains and surface vugs in the low-pressure stage (Peng et al., 2017). In this study, bulk samples were selected for the MIP experiment to reduce the conformance effect. Additionally, the PSD result measured by MIP during the low-pressure cycle (corresponding to pores>30 μm) was not considered to mitigate the error caused by conformance.

3.2.4 Low-temperature gas adsorption (LTGA)

Low-temperature N_2 adsorption (LTN_2A) and low-temperature CO_2 adsorption ($LTCO_2A$) were performed using the Autosorb-IQ analyzer produced by the Quantachrome Instruments to determine the PV, SA, and PSD. The shale sample was pulverized to a size of 100–150 μm. The crushed sample was dried in an oven at 110℃ for 24 h to mitigate the influence of free water and volatile gases. The LTN_2A was conducted at 77.35 K and the relative pressure (P/Po) was set within the scope of 0.005–0.996. The Brunauer-Emmett-Teller (BET) theory and Barrett-Joyner-Halenda (BJH) model were adopted to calculate the PV and SA (Brunauer et al., 1938; Barrett et al., 1951). $LTCO_2A$ was implemented at 273 K, and the P/Po was set within the scope of 0.00001–0.032. The PV and SA were calculated using the density functional theory (DFT) in $LTCO_2A$ (Lowell et al., 2012).

3.2.5 Image analysis

The pore morphology was characterized numerically via image analysis. High-resolution images obtained by the FE-SEM observation were analyzed by Image-Pro Plus (IPP) software developed by Midia Cybernetics. Through spatial calibration, filtering, thresholding, and segmentation, features of different pores were extracted including, but

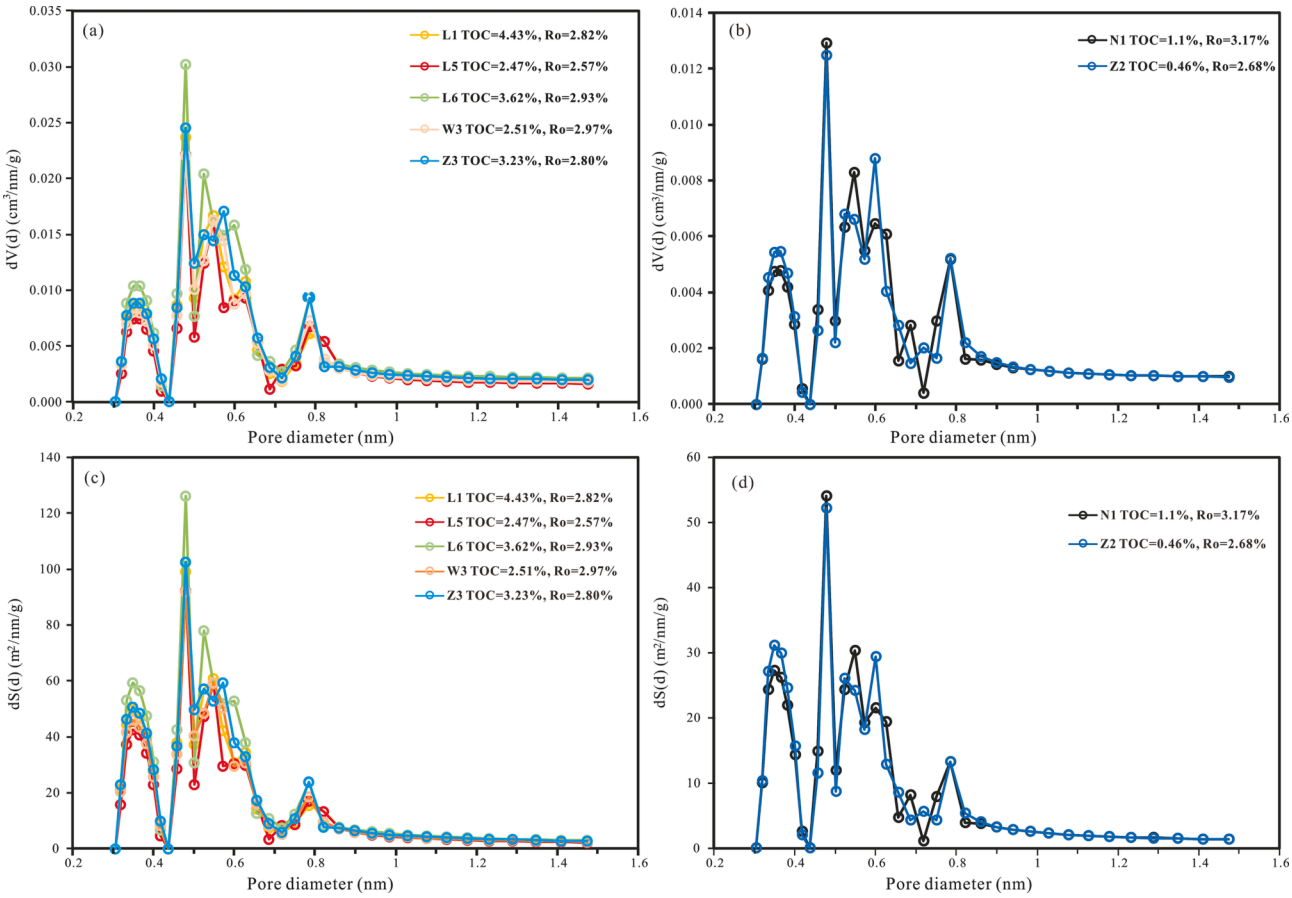

Fig. 9. The characteristics of PSD of the Longmaxi shale in the study area obtained by LTCO$_2$A.

not limited to, pore area, perimeter, diameter, and number (Chandra and Vishal, 2021). For some large-scale discernible pores, the method of Artificial Identification of Area of Interests (AOI) was also adopted. The theory underpinning the relationship between pore area (S) and equivalent perimeter (P) and fractal dimension (D) was proposed by Voss et al. (1991). It formed the basis of the discussion regarding the heterogeneity of different pore types, which is shown below:

$$\lg P = \frac{D}{2} \times \lg S + C \quad (3)$$

The area of shale component (OM, brittle mineral, clay mineral, and pyrite) and corresponding pores was extracted from FE-SEM images to investigate the PV of different pore types (Gao et al., 2021). Moreover, abundant representative FE-SEM images of each component were selected for calculating the PV to avoid the influence of the heterogeneity of the bulk sample and make each component more representative. The volume fraction of each component in shale was determined by mass fraction and corresponding density, as shown in Eq. (4). The mass fraction of OM and mineral composition were obtained from the TOC content and XRD analysis. This integrated imaging and compositional method can quantitatively characterize the shale PV. However, it should be noted that this method is limited by the abundance of FE-SEM images.

$$\phi_i = \frac{m_i}{\rho_i} \cdot \left(\sum_{i=1}^{4} \frac{m_i}{\rho_i} \right)^{-1} \quad (4)$$

where φ_i is the volume fraction (%), $i = 1, 2, 3, 4$ (i represents OM, brittle mineral, clay mineral, and pyrite, respectively); m_i represents the mass fraction of each component (%); ρ_i is the density of each component (g/cm^3), and the densities of OM, brittle mineral, clay mineral, and pyrite are 1.26, 2.675, 2.7, and 4.9, respectively (Gao et al., 2021).

According to the sum of the extracted areas of different pore types and their corresponding component areas, the surface porosity of different components could be obtained (Gao et al., 2021). Then, the PV of each component was calculated by Eq. (5), as shown below.

$$V_{pore(i)} = \phi_i \cdot \Phi_i \cdot \frac{1}{\rho} \quad (5)$$

where $V_{pore\ (i)}$ represents the PV per gram of each shale component (cm^3/g); Φ_i is the surface porosity of each shale component (%); ρ is the bulk density obtained by MIP (g/cm^3).

4 Results

4.1 Organic geochemistry

As illustrated in Table 1 below, the TOC contents of the Longmaxi shale are 0.42–4.67%, with an average of 2.69%. Solid bitumen displays a rougher surface, weaker anisotropy, and lower random reflectivity, making it a good target for reflectance measurements (Luo et al., 2018). The EqRo values are 2.23–3.17%, with an average of 2.8%, indicating that the Longmaxi shale is at the over-mature stage (Table 1).

The FE-SEM observation shows that the OM of the Longmaxi shale mainly consists of migrated bitumen and non-granular graptolites, which are characterized as irregular strips and blocks and dispersed within the mineral matrix (Fig. 2a). Migrated bitumen predominantly manifests as fine void-filling (Teng et al., 2022; Liu et al., 2022; Fig. 2b) and is mixed with clay minerals (Fig. 2c). Graptolites are well preserved in the Longmaxi shale (Fig. 2d and e), which typically present as parallel periderm and segmentation, with occasional pyrite filling (Fig. 2f).

4.2 Mineral composition

The mineral components are summarized in Table 1, including quartz, clay minerals, feldspar (potassium feldspar and plagioclase), carbonate minerals (calcite and dolomite), and pyrite. The quartz content in the Longmaxi shale is relatively high, ranging from 29.6% to

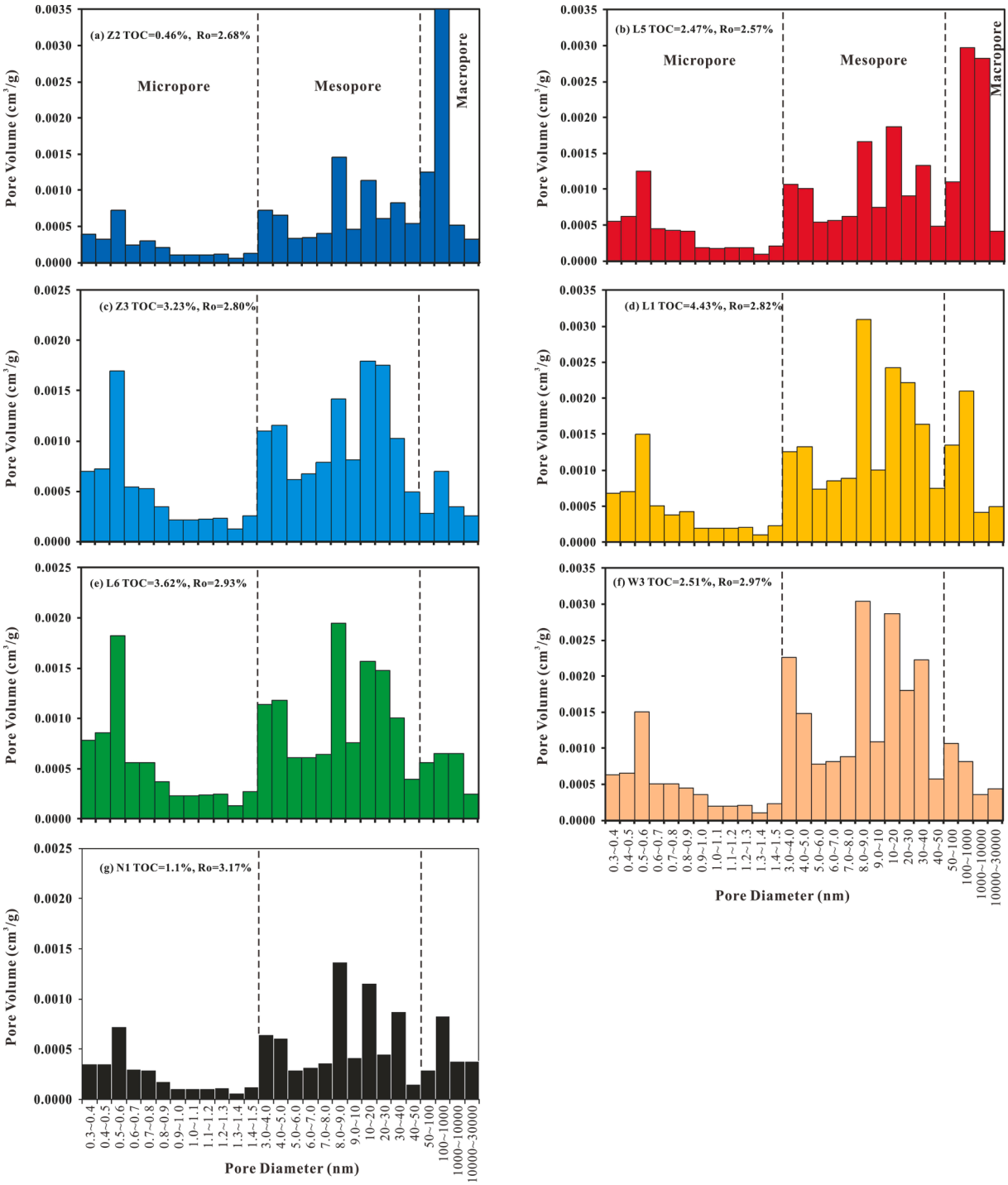

Fig. 10. Full-scale PSD of the Longmaxi shale in the southern part of the Sichuan Basin.

64.9%, with an average of 39.4%. The feldspar content accounts for 2.7–20.8%, with an average of 6.78%. Quartz and feldspar are mostly euhedral-granular (Fig. 3a and b). Moreover, the authigenic quartz cement mixed with migrated bitumen and clay minerals can be observed (Peng et al., 2020b; Fig. 3c). The carbonate mineral content varies from 3.3% to 34.1%, with an average of 13.9%. The clay mineral content accounts for 18.1–51.5%, with an average of 36.7%, including illite, chlorite, and illite–smectite (I/S) layer. The relative content of illite ranges from 63% to 78%, with an average of 69.6%. The lithofacies of the Longmaxi shale can be distinguished based on the TOC content and mineral composition (Fig. 4). The OM-rich and OM-poor shales in the Longmaxi Formation are mainly siliceous and mixed shale. The OM-moderate shale is mainly argillaceous shale, containing siliceous and mixed shale. Furthermore, pyrite is identified as rather common in the Longmaxi shale, with a content of 1.4–9.3%. It is primarily composed of pyrite framboids (Fig. 3d), with rare elements of euhedral pyrite (Fig. 3e). The clay minerals are mostly distributed within the mineral matrix in the form of layers, strips, worms, and fine sheets (Fig. 3b, c, and f), with strong plasticity, which are easily compacted or mixed with OM and pyrite (Fig. 3g).

4.3 Pore types

The pore types of the Longmaxi shale in the study area were

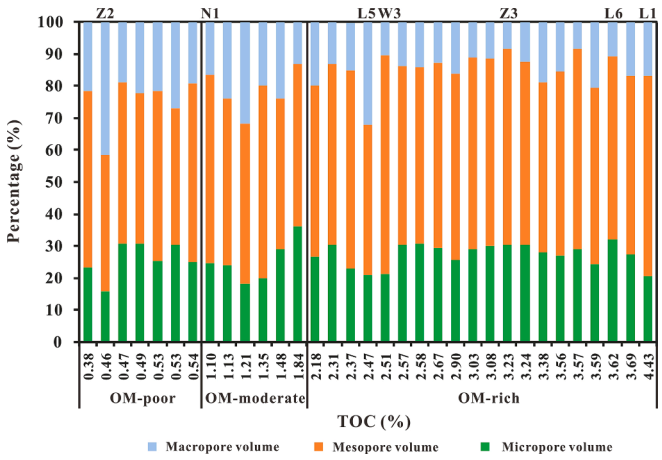

Fig. 11. The percentage of micropore, mesopore, and macropore volumes in the total pore volume of the Longmaxi shale (The red circle represents the data used in this study, and other data are obtained from Lyu et al. (2020) and Wang et al. (2020)). (For interpretation of the references to colour in this figure legend, the reader is referred to the web version of this article.)

examined by FE-SEM observations. The pores are mostly comprised of intraparticle (intraP), interparticle (interP), and OM pores. IntraP pores are found within mineral particles or grains, while interP pores are located between mineral particles and clay flakes (Slatt and O'Brien, 2011). OM pores are developed within OM with increasing thermal maturity (Loucks et al., 2012; Pommer and Milliken, 2015).

4.3.1 IntraP pores

Based on the FE-SEM observation, intraP pores found in the Longmaxi Formation are seen to be developed over a broad size distribution, ranging from several nanometers to micrometers. IntraP pores are predominantly related to dissolution, pyrite framboids, or brittle mineral fracturing (such as feldspar and calcite). Dissolution pores generally appear as (1) round, dispersed pores ranging from a few microns to several hundred microns (Fig. 5a), and (2) larger-scale irregular pores, which are readily filled by migrated bitumen or clay minerals (Fig. 5b). Intercrystalline pores within pyrite framboids are invariably found to be caused by incomplete lattice development or dissolution (Fig. 5c). The microcracks formed by brittle mineral fracturing are mostly distributed along the mineral cleavage along with the largest PSD (Fig. 5d). These are hypothesized to be highly significant constituents of the shale pore system, but they are also deemed to have been easily filled by authigenic cement.

4.3.2 InterP pores

As mentioned above, interP pores are mainly found to be subdivided into pores between different mineral particles and pores among clay flakes (Slatt and O'Brien, 2011; Ibad and Padmanabhan, 2022). The former is inherited from inherent pores and is mostly linear or polygonal along the borders of brittle minerals (Fig. 5e). The latter mainly results from the non-parallel arrangement of flakes or the filling of other particles (Fig. 3h, Fig. 5f).

4.3.3 OM pores

The evolution of OM pores is controlled by the types, abundance, and thermal maturity of OM (Milliken et al., 2013). The OM in the Longmaxi shale mainly consists of types I-II$_1$ kerogen, which favors the formation of OM pores (Cao et al., 2021). Previous studies have investigated the evolution of OM pores with different morphologies during thermal evolution (Mathia et al., 2016; Ko et al., 2018; Cao et al., 2022). Fig. 6 below generally illustrates that OM pores proliferate from sporadic micropores to developed large-scale cheese-like pores with increasing TOC content and maturity.

In order to more intuitively reveal the evolution of OM pores with increasing maturity, OM pores are subdivided into four types according to the pore size and morphology under the visible range of SEM resolution, while those smaller than 5 nm are difficult to distinguish using SEM observations (Fig. 6a). Bubble OM pores are characterized by round shapes with pore sizes of 5–100 nm. They are independent and densely distributed (Fig. 6b). Sponge-like OM pores are developed sporadically, characterized by irregular edges with pore sizes of 100–350 nm (Fig. 6c

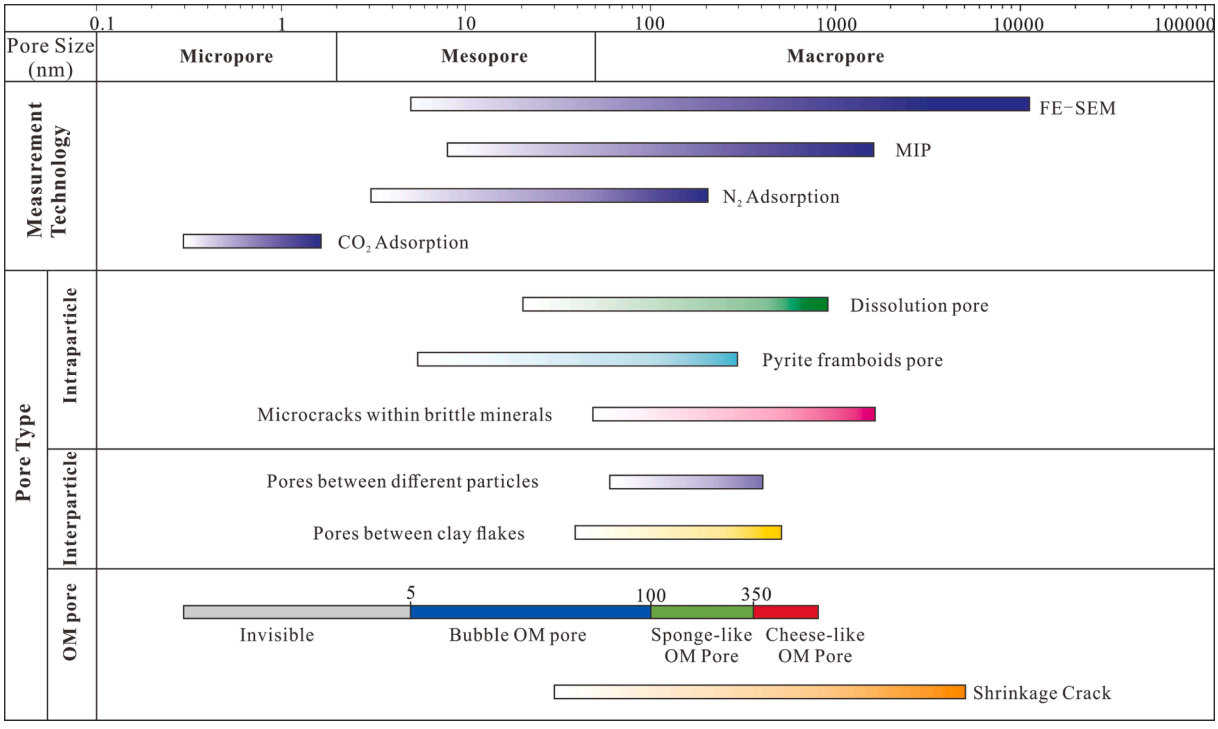

Fig. 12. Measurement ranges of different techniques integrated in this study and the PSD of different pore types.

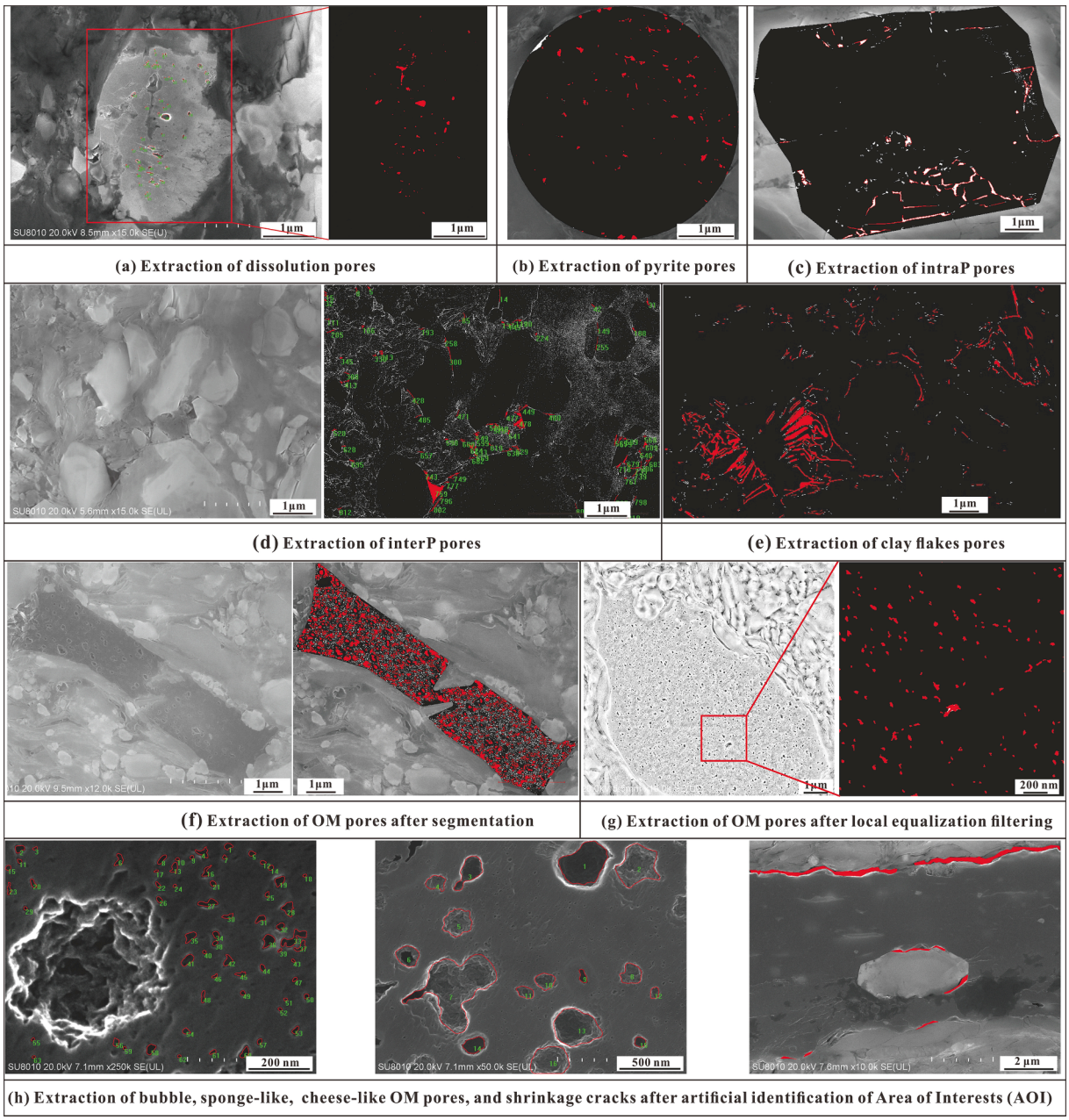

Fig. 13. Image analysis of different pore types using IPP software. (a–c) the extraction of intraP pores from Fig. 5a, c, and d; (d–e) the extraction of interP pores from Fig. 3g; (f–h) the extraction of OM pores from Fig. 6d, e, h, and i.

and d). In shale with higher TOC content and maturity, cheese-like OM pores are formed by connecting sponge-like OM pores, which are more irregular in the shape with pore sizes>350 nm (Fig. 6e–g). In shale with medium TOC content and extremely high thermal maturity (Ro > 3.0%), bubble OM pores are the most developed (Fig. 6h). Compared with bubble, sponge-like, and cheese-like OM pores, shrinkage cracks form along the interface between OM and minerals and are distributed in strips, with sizes ranging from tens of nanometers to several microns (Fig. 6i). Interestingly, increased magnification enables the first three types of OM pores with completely different pore sizes to coexist within the same field of view (Fig. 6d–f), forming an organic pore system. This classification of OM pores is conducive to the subsequent study on the evolution of pore types and the changes in the relative contributions of different pore types.

4.4 Pore structure

The pore structure parameters of the Longmaxi shale obtained by MIP and LTGA are illustrated in Table 2 below. According to the International Union of Pure and Applied Chemistry (IUPAC) classification, pore sizes are subdivided into micropores (<2 nm), mesopores (2–50 nm), and macropores (>50 nm).

4.4.1 MIp

The MIP experiment can quantify the shale pore structure, especially for mesopores and macropores (Bustin et al., 2008; Clarkson et al., 2013). As shown in Table 2, the porosity obtained by MIP tests varies from 2.59% to 7.02%, with an average of 4.82%. The PV ranges from 0.01 to 0.027 cm^3/g, with an average of 0.019 cm^3/g. Two types of pore structures are revealed within the study area. As shown in Fig. 7a, the mercury injection quantities of five samples increase slowly with

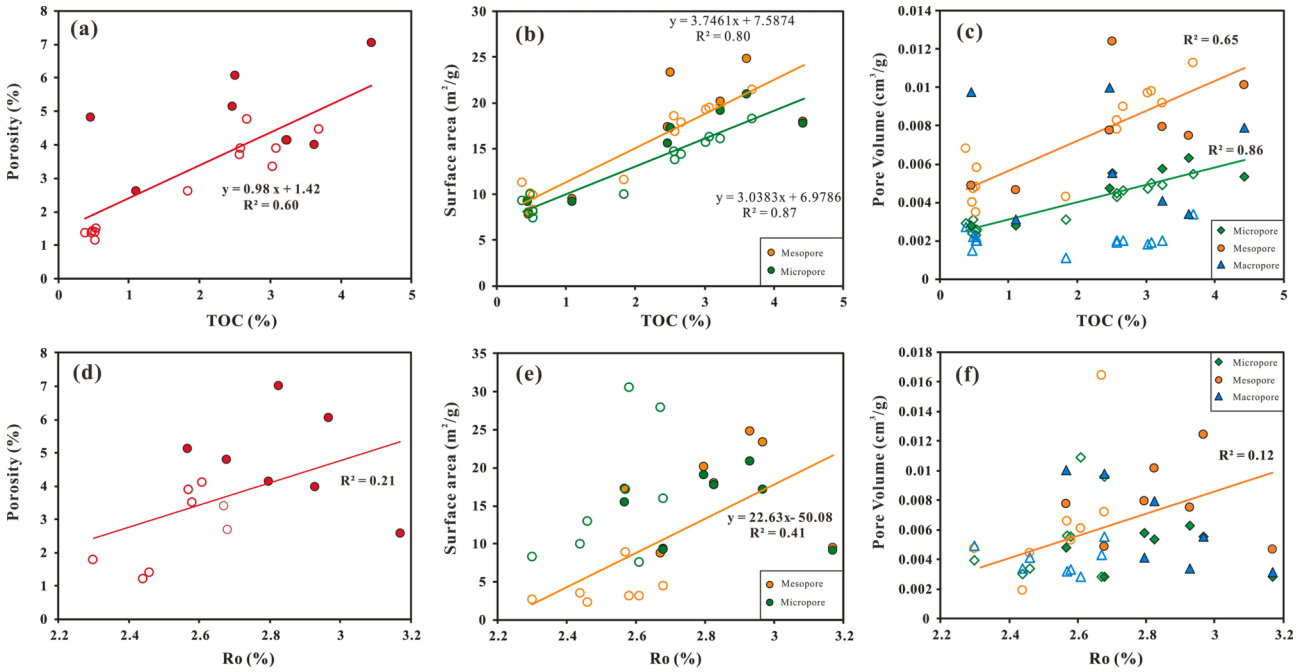

Fig. 14. (a–c) Relationship between TOC and porosity, SA, and PV; (b–d) Relationship between Ro and porosity, SA, and PV in over-mature Longmaxi shale (The solid circle, triangle, and diamond represent the data obtained in this paper. The hollow circle, triangle, and diamond are obtained from Lyu et al. (2020) and Jiang et al., (2016)).

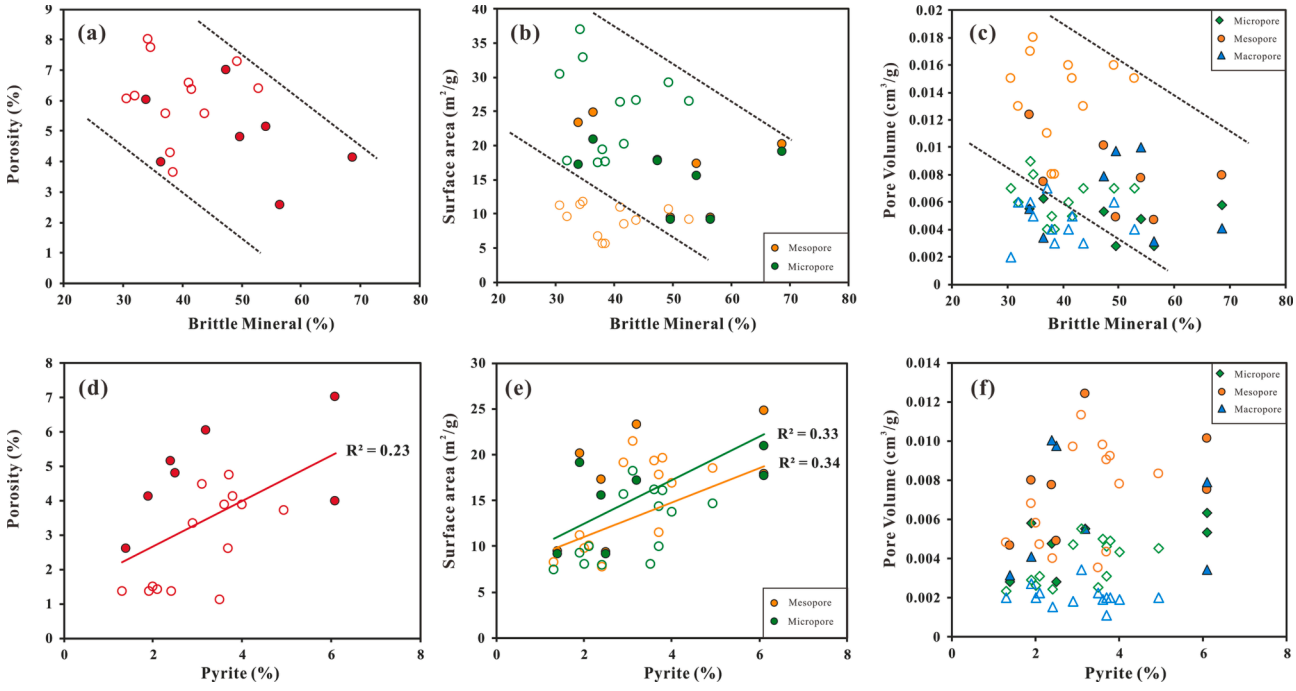

Fig. 15. Relationship between mineral contents, porosity, SA, and PV in over-mature Longmaxi shale (The solid circle, triangle, and diamond represent the data obtained in this paper. The hollow circle, triangle, and diamond are obtained from Lyu et al. (2020) and Wang et al., (2020)).

pressure (<60 MPa) and then increase rapidly (>60 MPa), indicating that pores are mainly concentrated in the range of 20–50 nm, and they consist of mesopores. Until reaching the maximum pressure, the mercury injection quantities are not saturated and still keeps rising, signifying that an abundance of pores < 8 nm exists in the samples. The mercury injection quantities of L5 and Z2 increase rapidly when the pressure reaches 0.5 MPa and 2 MPa, respectively, indicating that the pores are concentrated in the range of 10 nm–2 μm and 10–500 nm, respectively, and they consist of mesopores and macropores (Fig. 7b).

4.4.2 Low-temperature N_2 adsorption (LTN_2A)

The BET SA calculated by LTN_2A of seven shale samples varies from 9.39 to 24.83 m^2/g, with an average of 17.5 m^2/g. The BJH PV varies from 0.006 to 0.015 cm^3/g, with an average of 0.009 cm^3/g (Table 2). According to the IUPAC classification, the adsorption isotherms of the Longmaxi shale present as type IV, with obvious hysteresis loops and no

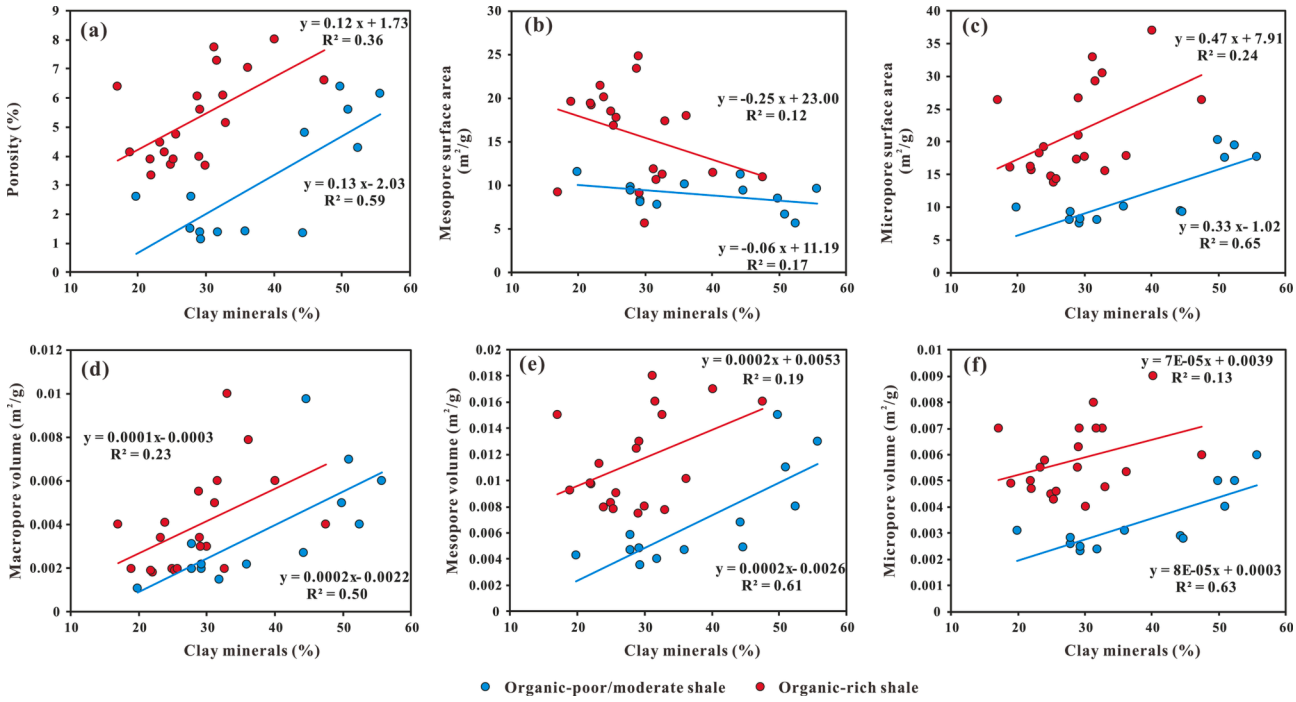

Fig. 16. Relationship between clay minerals, porosity, SA, and PV in OM-poor/moderate and OM-rich Longmaxi shale, showing that clay minerals control the pore properties in OM-poor/moderate shale (Part of the data obtained from Lyu et al. (2020) and Wang et al. (2020)).

saturated adsorption platform, indicating the process of capillary condensation and the presence of macropores (Fig. 8a and b). The hysteresis loops are mainly type H_3, corresponding to the silt-shaped pores. The adsorption volumes of shale samples with a high TOC content (Fig. 8a) are larger than those of shale samples with a low TOC content (Fig. 8b). The adsorption/desorption isotherms of samples W3 and L1 are steeper (when P/Po > 0.8), indicating the existence of ink-bottle-like pores (Fig. 8a). As shown in Fig. 8c and d below, the PV and SA are primarily comprised of mesopores between 3 and 40 nm and 3–20 nm respectively, and gradually decrease with increasing pore diameter. Pore structure parameters in OM-poor/moderate shale samples (N1 and Z1) are found to be significantly lower than those in high TOC samples, indicating that the TOC content could observably affect the PV and SA.

4.4.3 Low-temperature CO_2 adsorption ($LTCO_2A$)

The DFT SA calculated by $LTCO_2A$ of seven shale samples is 9.18–20.92 m^2/g, with an average of 15.56 m^2/g. The DFT PV is 0.003–0.006 cm^3/g, with an average of 0.005 cm^3/g (Table 2). Fig. 9 below exhibits similar characteristics of pore structure with a pore size < 2 nm, mainly distributed over three intervals: 0.3–0.4 nm, 0.45–0.7 nm, and 0.75–0.9 nm, respectively. The PV and SA of OM-rich shale samples (Fig. 9a and c) are found to be significantly higher than those of OM-poor/moderate samples (Fig. 9b and d), which is consistent with the conclusion drawn using LTN_2A.

4.5 Full-scale pore size distribution

Considering the measurement ranges of different methods, the micropores (0.3–1.5 nm), mesopores (3–50 nm), and macropores (>50 nm) can be well characterized by $LTCO_2A$, LTN_2A, and MIP experiments, respectively (Mastalerz et al., 2013; Wang et al., 2020; Chen et al., 2021; Zhao et al., 2022). In this study, the correlation between the PV and pore size was used to investigate the PSD of the Longmaxi shale. As illustrated in Fig. 10 below, micropore PV is mainly contributed by pores between 0.5 and 0.6 nm. Mesopore PV is mainly contributed by pores between 8 and 40 nm. Macropore PV is mainly contributed by pores between 100 and 1000 nm and>30 μm. The PV values of micropores and mesopores are comparable with those obtained by $LTCO_2A$ and LTN_2A, while the PV values of macropores are smaller than that obtained by MIP. It is mainly because the PV of pores smaller than 50 nm and those>30 μm measured using the MIP experiments were excluded in order to reduce the conformance effect.

Previous studies have found that mesopores contributed the most to the PV in over-mature Longmaxi shale, with micropores and macropores also contributing a certain amount to PV (Jiang et al., 2016, 2020; Lyu et al., 2020; Wang et al., 2020; Li et al., 2022b). OM-poor/moderate shale presents a higher proportion of macropore volume than OM-rich shale, indicating that larger inorganic pores are developed in the low TOC shale, which is consistent with FE-SEM observations (Fig. 10a; Fig. 11). As the TOC content and maturity increase, the macropore volume gradually decreases, and the mesopore volume is the most developed, and there is only a slight change in the micropore volume (Fig. 10b–f; Fig. 11). In addition, the PV of the N1 sample decreases significantly because of its low TOC content and high maturity (Fig. 10g).

4.6 Extraction of pore parameters of different pore types

Fig. 12 below summarizes the measurement ranges obtained by different experimental methods (Arif et al., 2021). In this study, multi-scale methods were integrated to characterize the pore structures, PSD, and pore types. IntraP pores have a wide PSD, which ranges from several nanometers to microns. In contrast, the PSD of interP pores is more concentrated, varying from tens of nanometers to 500 nm. The visible OM pores are mainly concentrated at 5–750 nm, while the invisible OM pores obtained by the $LTCO_2A$ experiment are mostly concentrated at 0.5–0.6 nm. OM shrinkage cracks exhibit irregular shapes and the widest PSD than other pore types. Additionally, the parameters of different pore types were extracted from high-resolution FE-SEM images by image analysis using IPP software. Fig. 13 displays several representative images of different pore types after image processing. The grayscale SEM images were filtered to remove artifacts and then were transformed into binary images by thresholding. Finally, the features of different pore types were extracted after segmentation.

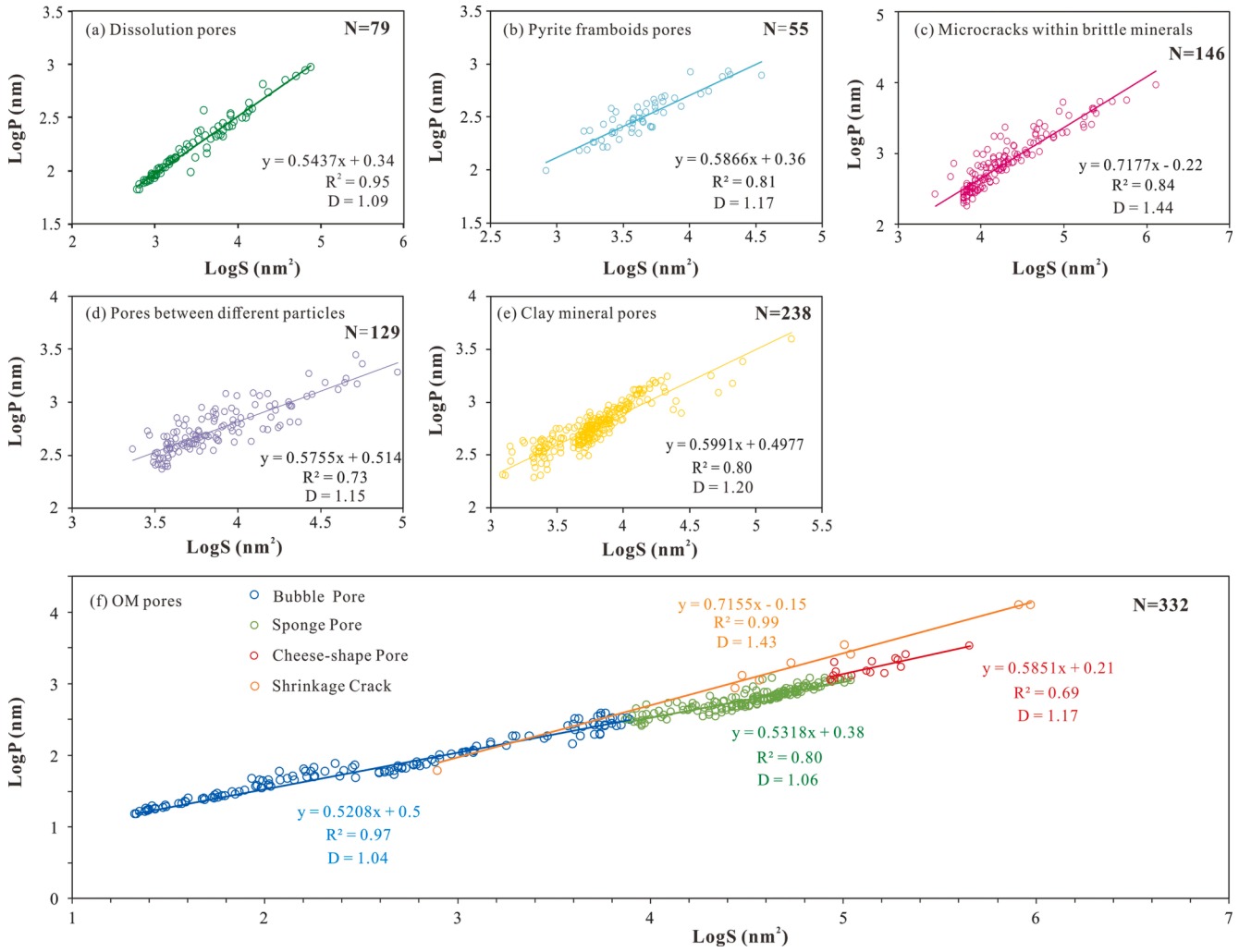

Fig. 17. Fractal characteristics of different pore types obtained by image analysis (The area (s) and perimeter (P) of different pore types show good correlations, showing that the D values of pores are reliable).

5 Discussion

5.1 Multi-factorial influences of different factors on shale porosity and pore structure

5.1.1 Influence of TOC and Ro on shale porosity and pore structure

Fig. 14 below illustrates the relationships between TOC, Ro, porosity, SA, and PV, respectively. Prominent positive correlations are identified between TOC and porosity (Fig. 14a). The SA and PV of micropores and mesopores also show positive correlations with TOC, while the macropore volume is randomly distributed with the increasing TOC content (Fig. 14b, c). These demonstrate the contribution of OM pores to the porosity, SA, and PV of mesopores and micropores in over-mature Longmaxi shale. Milliken et al. (2013) found an obvious positive relationship between TOC and porosity in two sets of Marcellus shale with maturities of 1.0% and 2.1%, respectively. However, when the TOC content was over 5.6%, this covariation disappeared in the lower-maturity shale and diminished in the higher-maturity shale, indicating that the thermal maturity may affect this correlation. A slight positive correlation is identified between Ro and porosity (Fig. 14d). Ro has a good correlation with mesopore SA, but is independent of PV (Fig. 14e, f). When Ro > 3%, the porosity, SA, and PV generally decreases, and the influence of other factors on shale physical properties is found to be masked by maturity (Mastalerz et al., 2013). After screening out shale samples with the maturity>3%, the correlation coefficient (R^2) between Ro and porosity, and the SA and PV of mesopores can be increased to 0.53, 0.68, and 0.34, respectively. Consequently, in over-mature shale (Ro > 2%), the TOC content and maturity greatly affect shale porosity and pore structure (Mastalerz et al., 2013; Bousige et al., 2016), especially the TOC content (Cao et al., 2015). Abundant OM is revealed to greatly improve the shale pore structure, develop more OM pores, and form more micropores and mesopores.

5.1.2 Influence of mineral composition on shale porosity and pore structure

The mineral composition of shale can significantly affect the porosity and pore structure of shale reservoirs (Mastalerz et al., 2013; Peng et al., 2020a, b). IntraP and interP pores related to minerals are essential constituents of the shale pore system. Brittle mineral contents show weak negative correlations with the porosity, SA, and mesopore volume, and no correlation with the PV of micropores and macropores, indicating that the pores related to brittle minerals contribute less to the porosity and pore structure of the Longmaxi shale (Fig. 15a–c). In OM-rich Longmaxi shale, pyrite has slight positive correlations with porosity and SA, but no correlation with PV, indicating the contribution of intercrystalline pores within pyrite framboids to shale pore space (Fig. 15d–f). The relationships between clay minerals and shale pore properties vary greatly in OM-rich and OM-poor shales (Lyu et al., 2020). In OM-poor/moderate Longmaxi shale, clay mineral contents correlate positively with the porosity, micropore SA, and PV (Fig. 16). Whereas these positive correlations decrease in OM-rich shale,

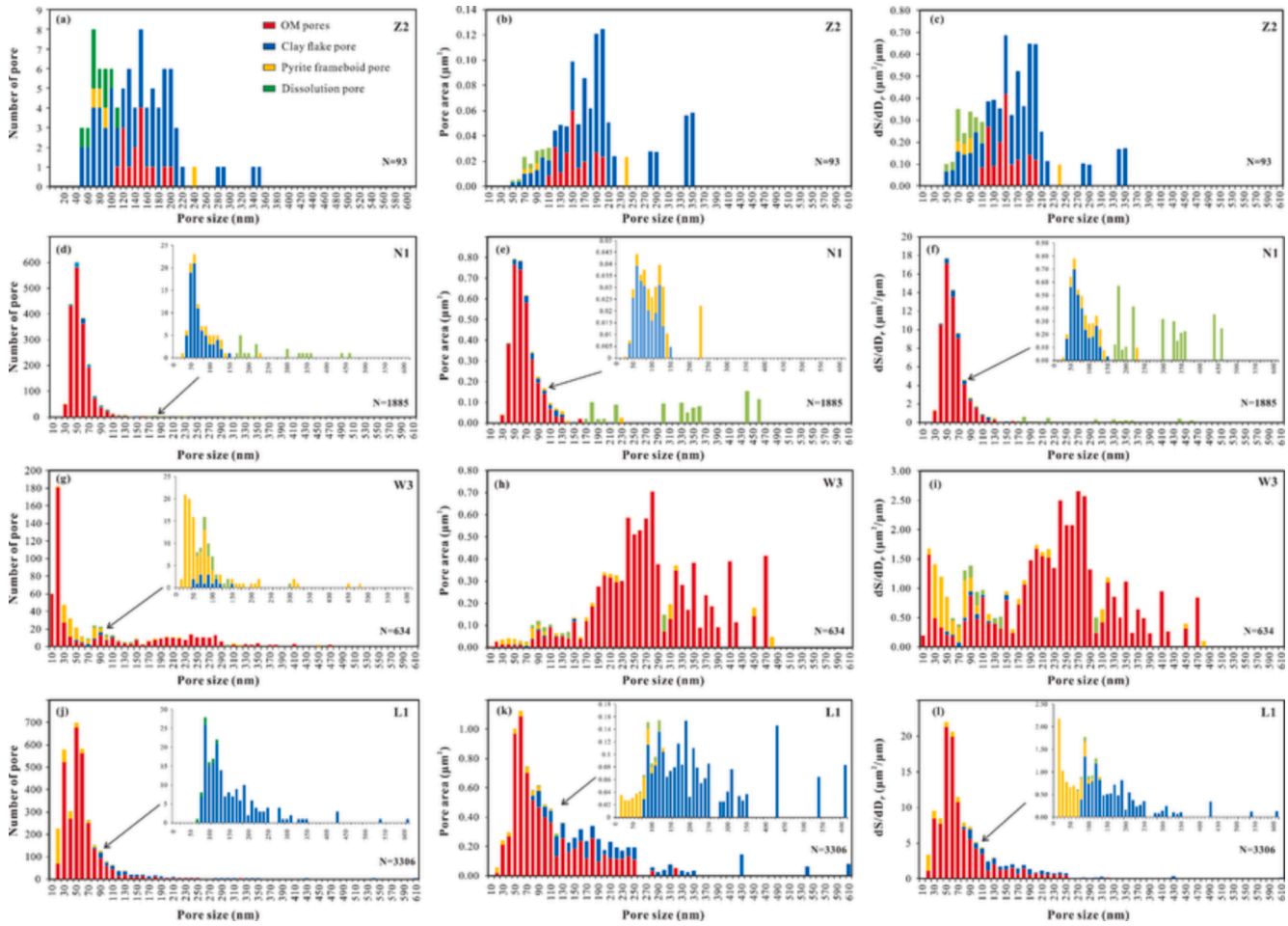

Fig. 18. Number, pore area, and dS/dD distribution of different pore types obtained by image analysis (a, b, and c are from Z2, TOC = 0.46%; d, e, and f are from N1, TOC = 1.1%; g, h and i are from W3, TOC = 2.51%; j, k and l are from L1, TOC = 4.43%).

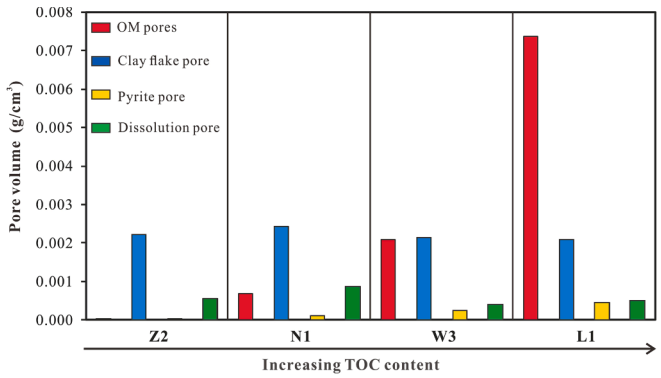

Fig. 19. The PV of different pore types of the Longmaxi shale.

signifying that clay mineral pores contribute to pore space in OM-poor/moderate shale.

5.2 Heterogeneity of different shale pore types

Different pore types share strong self-similarities and obvious fractal characteristics. Previous studies have investigated the fractal characteristics of nanopores in the Longmaxi shale using the fractal Frenkel-Halsey-Hill (FHH) method based on the LTN_2A isotherms and found that TOC content had a positive correlation with D values (Yang et al., 2014; Peng et al., 2019; Li et al., 2022b). However, the D values of different pore types fail to be characterized by the FHH model.

In this study, the D values of shale pores are obtained by image analysis, which range from 1.04 to 1.44, and the corresponding R^2 values range from 0.69 to 0.99 (Fig. 17). IntraP pores mainly consist of mesopores and macropores. The D values of dissolution pores, pyrite framboid pores, and microcracks within brittle minerals are 1.09, 1.17, and 1.44, respectively, revealing that the pore morphology of these three types of intraP pores is complex and heterogeneous (Fig. 17a–c). The pore size of interP pores is dominated by macropores. Compaction and recrystallization result in an irregular pore morphology among grains and/or crystals, the D value of which is 1.15, and the R^2 value is 0.73 (Fig. 17d). The D value of clay mineral pores is 1.2 (Fig. 17e). OM pores comprise a wide PSD range, greatly contributing to micropores, mesopores, and macropores. The D values of bubble OM pores, sponge-like OM pores, cheese-like OM pores, and shrinkage cracks are 1.04, 1.06, 1.17 and 1.43, respectively (Fig. 17f). OM pore heterogeneity is shown to increase with the increasing pore size (Peng et al., 2019). Although OM shrinkage cracks are highly heterogeneous, they could well connect OM pores and mineral-related pores, forming a complex organic–inorganic pore-fracture system, which is conducive to oil and gas migration (Zhang et al., 2016). Overall, OM pores are found to be the most homogeneous, followed by interP pores, while intraP pores present the greatest heterogeneity, which is consistent with earlier study findings obtained using box-counting fractal methods (Wang et al., 2016). Note that pore complexity and heterogeneity of shale reservoirs are also affected by multiple factors, such as TOC content, mineral composition, and tectonic movements (Peng et al., 2019).

Table 3
Parameters of different components of over-mature Longmaxi shale.

Sample ID	Component	Area (μm^2)	Pore area (μm^2)	Porosity (%)	Mass fraction (%)	Density (g/cm^3)	Volume fraction (%)	Volume (cm^3/g)	Pore volume (cm^3/g)
Z2	OM	64.47	0.23	0.36	0.46	1.26	1.02	0.003812	0.000014
	Clay mineral	52.75	0.68	1.29	44.60	2.70	45.97	0.172483	0.002223
	Pyrite	17.25	0.04	0.21	2.50	4.90	1.42	0.005327	0.000011
	Brittle mineral	15.10	0.04	0.28	49.60	2.68	51.60	0.193612	0.000551
N1	OM	54.74	3.64	6.65	1.10	1.26	2.68	0.010121	0.000673
	Clay mineral	11.81	0.24	2.03	27.80	2.70	31.64	0.119362	0.002425
	Pyrite	3.10	0.11	3.49	1.40	4.90	0.88	0.003312	0.000115
	Brittle mineral	524.1	1.86	0.35	56.40	2.68	64.80	0.244422	0.000867
W3	OM	97.58	6.90	7.07	2.51	1.26	7.67	0.029691	0.002099
	Clay mineral	3.65	0.05	1.34	28.80	2.70	41.05	0.158985	0.002134
	Pyrite	20.43	0.49	2.40	3.20	4.90	2.51	0.009734	0.000234
	Brittle mineral	83.04	0.18	0.22	33.90	2.68	48.77	0.188887	0.000409
L1	OM	22.52	4.36	19.36	4.43	1.26	9.80	0.038016	0.007360
	Clay mineral	151.7	2.18	1.44	36.20	2.70	37.36	0.144972	0.002084
	Pyrite	8.33	0.28	3.30	6.10	4.90	3.47	0.013461	0.000445
	Brittle mineral	157.8	0.41	0.26	47.40	2.68	49.38	0.191599	0.000498

5.3 Contribution of pore types to pore space

5.3.1 Relative contribution of pore types to pore area

By discussing influencing factors and heterogeneity of the shale pore structure, the pores related to OM (except for shrinkage cracks), pyrite framboid, clay mineral, and dissolution seem to be the main contributors to shale pore space. Based on abundant SEM observations and image analysis, four typical samples with different TOC contents and maturities were used to analyze the pore number, diameter (D_P), pore area (S), and dS/dD_P of different pore types to determine the contribution of pore types to pore area, as shown in Fig. 18. Note that in order to reduce the influence of data collection number and the limited FE-SEM observation range of the whole sample, pore area and dS/dD_P were adopted together to characterize the relative contribution of pore types to pore area (Tian et al., 2020). The number and SA of pores increase significantly with the TOC content (Fig. 18). For OM-poor shale (Z2), the number and area of pores that can be extracted are significantly less than in OM-rich/moderate shale (Fig. 18a–c). Clay mineral pores contribute more to the pore area, followed by OM pores and dissolution pores, and finally pyrite framboid pores. With the increasing TOC content and maturity, the relative contribution of OM pores to the pore area is gradually highlighted (Fig. 18d–l). The sample N1 (Ro = 3.17%) has a limited PSD (mainly 40–90 nm). The bubble OM pores contribute the most to the pore area in sample N1, and a small number of large-scale dissolution pores also contribute to the pore area (Fig. 18d–f). The sample W3 has a wide PSD, with the largest number of bubble OM pores found in the range of 10 to 20 nm, and sponge-like and cheese-like OM pores in the range of 190 to 470 nm contributing the most to the pore area, followed by bubble OM pores and pyrite framboid pores (Fig. 18g–i). For sample L1 with a high TOC content, the number of bubble OM pores is most abundant, and OM pores (40–120 nm) are the main contributor to the pore area (Fig. 18j–l).

5.3.2 Relative contribution of pore types to pore volume

The contribution of different pore types to the PV varies significantly. In this study, the PV of OM pores, clay mineral pores, pyrite framboid pores, and dissolution pores of four samples was obtained (Fig. 19), and the detailed parameters are listed in Table 3. Notably, due to the limitations of FE-SEM images, the PV here failed to represent the total PV of the whole shale sample. However, the relative contribution of different pore types to the PV is still valid because the relative abundance and surface porosity of each component are taken into account. In the OM-poor shale (sample Z2), the PV is mainly contributed by clay mineral pores, followed by dissolution pores, but without the contribution of OM pores. The relative contribution of OM pores to the PV increases with the increasing TOC content (Li et al., 2022b). In the OM-rich shale sample L1, OM pores account for 70% of the PV, clay mineral pores account for 20%, and pyrite framboid pores and dissolution pores account for 10%. Interestingly, the PV of pyrite framboid pores increase with the increasing TOC content, indicating that OM provides favorable conditions for the development of pyrite framboids (Berner, 1984; Rigby et al., 2006).

5.4 Contribution evolution of pore types to shale pore space

Both the processes of diagenesis and hydrocarbon generation were found to influence intraP, interP, and OM pores, as previously contended by Mastalerz et al. (2013). The evolution of shale pores can be divided into three stages: immature (Ro < 0.5%), mature (Ro = 0.5–2.0%), and over-mature (Ro > 2.0%) (Cao et al., 2022). Based on previous studies, we conclude the pore evolution of the Longmaxi shale with type I-II_1 kerogen.

At the immature stage (Ro < 0.5%), the original porosity of loose sediments (biological skeleton, minerals, and OM) is very high, mainly consisting of interP pores (Pommer and Milliken, 2015; Cao et al., 2021; Fig. 20a). With mechanical compaction and chemical cementation, interP pores decrease significantly, while intraP pores (mainly pyrite framboids) increase (Milliken et al., 2014; Xu et al., 2021b; Fig. 20b, c).

When Ro = 0.5–2.0%, interP pores between different grains decrease continually (Fig. 20d), while clay mineral pores increase because of the transformation of smectite and kaolinite to flocculent I/S mixed layer when Ro > 1.0% (Burst, 1969; Fig. 20e). Affected by temperature and catalysis of clay minerals, oil, solid bitumen, migrated bitumen, and a few gases are generated by thermal degradation of kerogen (Ardakani et al., 2018; Liu et al., 2022), producing abundant dissolution pores, intragranular fractures, and small quantities of bubble OM pores (Jarvie et al., 2007; Wang, 2017; Xu et al., 2021a; Fig. 20f-h). Whereas solid bitumen blocks the large-scale inorganic pores first and then OM pores, significantly reducing the porosity and PV (Chuhan et al., 2000; Mathia et al. 2016; Xu et al., 2021b). In OM-rich shale, the condensation reaction of layered algae forms shrinkage cracks (Fig. 20i). When Ro > 1.6%, abundant bubble OM pores and sponge-like OM pores are developed (Tang et al., 2016; Fig. 20j and k), and the total PV decreases while the total SA increases rapidly (Zhang, 2020).

When Ro > 2.0%, OM pores are dominant and are mainly affected by the TOC content (Milliken et al., 2013). The size, scale, and connectivity

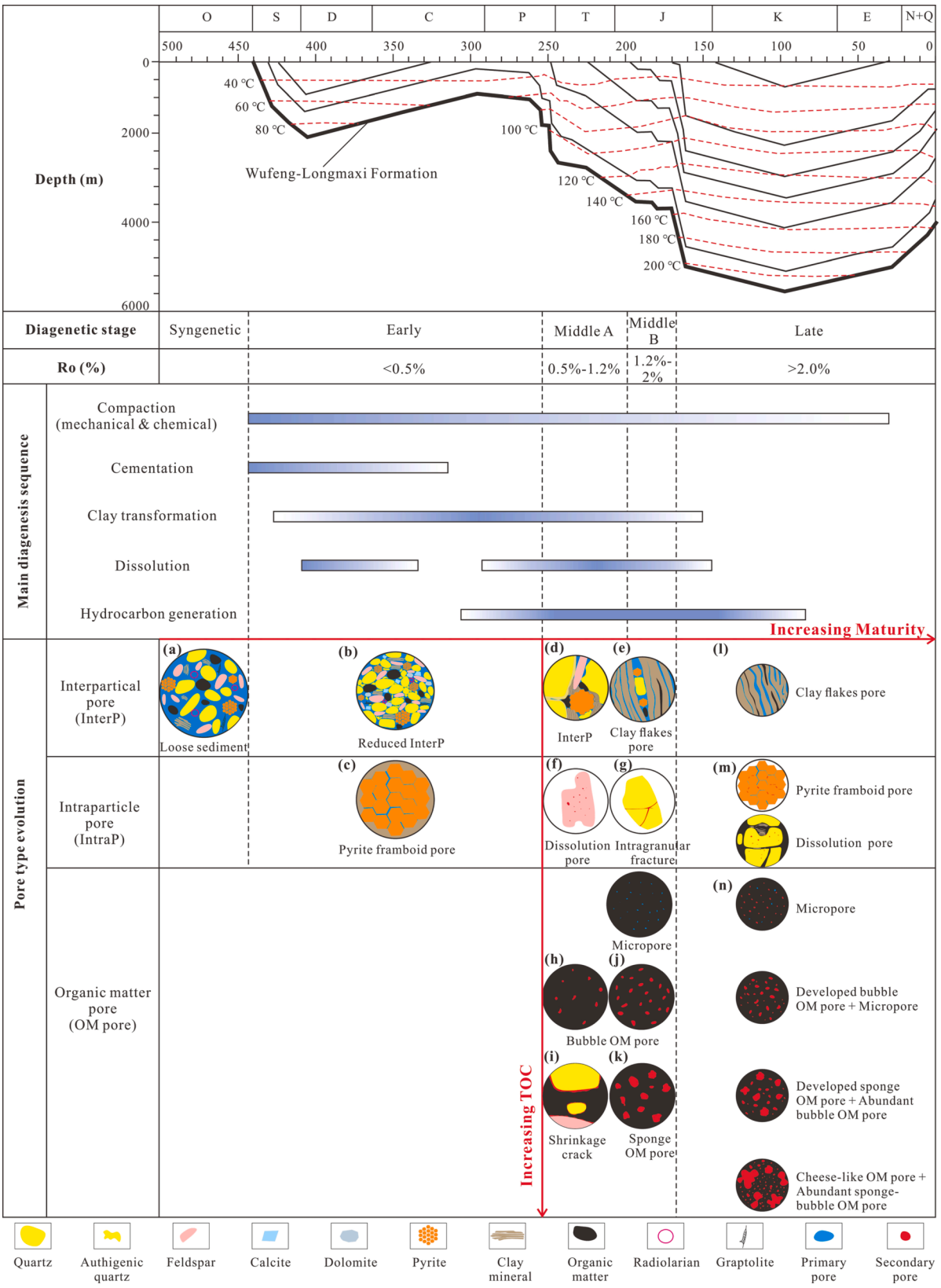

Fig. 20. Comprehensive model showing burial history, thermal history, and the corresponding evolution of pore types of the Longmaxi shale in the southern part of the Sichuan Basin (the burial and thermal histories modified from Xu et al., 2021a).

of OM pores increase with the increasing TOC content. Independently distributed bubble or sponge-like OM pores link up to form irregular cheese-like OM pores, which are conducive to shale gas adsorption (Xu et al., 2021a, b). In OM-poor shale, clay mineral pores are identified as playing a major role in pore space (Fig. 18; Fig. 19; Fig. 20l and m). Invisible OM pores beyond FE-SEM observations are the main contributors to micropores (Fig. 20n). In OM-rich/moderate shale, with the increasing TOC content and maturity, the OM pore system gradually develops from an assembly of invisible OM micropores, irregular bubble OM pores, and sporadic sponge-like OM pores to an assembly of invisible OM micropores, well-developed and uniformly distributed bubble OM mesopores, and widespread sponge-like and cheese-like macropores (Fig. 6d–f; Fig. 20n). OM pores contribute the most to pore space.

6 Conclusion

For over-mature Longmaxi shale, a quantitative method integrating XRD analysis, FE-SEM, MIP, LTGA, and image analysis was adopted to analyze the structure, physical properties, and influencing factors of different pore types. Eventually, the relative contribution of pore types to pore space was quantitatively characterized. The main conclusions obtained are as follows:

(1) Based on the FE-SEM observation, intraP, interP, and OM pores are found in the Longmaxi shale. OM pores can be subdivided into invisible micropores (<5 nm), uniformly distributed bubble pores (5–100 nm), independent and rounded sponge-like pores (100–350 nm), connected cheese-like pores (>350 nm), and shrinkage cracks.

(2) Full-scale pore size distribution obtained by MIP, LTN_2A, and $LTCO_2A$ exhibits that mesopores contribute the most to the PV. In OM-poor shale, macropores are relatively developed. Moreover, the physical properties of the Longmaxi shale are mainly affected by the TOC content. The TOC contents show strong positive correlations with the porosity, SA, and PV. Maturity and pyrite show slight positive correlations with the porosity, SA and PV of mesopores. In OM-poor/moderate shale, clay minerals show significantly positive correlations with porosity, micropores SA, and PV.

(3) The fractal dimensions (D) of different pore types were obtained by image analysis. The D values of intraP, interP, and OM pores are 1.09–1.44, 1.15–1.2, and 1.04–1.43, respectively. Higher D values indicate stronger heterogeneity.

(4) The number, diameter, and pore area of different pore types were extracted to quantitatively calculate the relative contribution of pore types to pore area and volume. In OM-poor Longmaxi shale, the contribution to the SA is in the order of clay mineral pores, OM pores, dissolution pores, and pyrite framboid pores. The contribution of OM pores to pore area becomes dominant with the increasing TOC content. Similarly, the PV is mainly contributed by clay mineral pores in OM-poor shale. The contribution of OM pores to the PV increases with the increasing TOC content.

(5) The contribution of pore types to shale pore space at different evolutionary stages was revealed based on previous studies. When Ro < 0.5%, interP pores are the main contributors to shale pore space, leading to a high original porosity. When Ro = 0.5–2.0%, intraP and OM pores dominantly contribute to pore space. When Ro > 2.0%, in OM-poor shale, clay mineral pores contributed the most to shale pore space. In OM-rich/moderate shale, with the increasing maturity, an assembly of invisible OM micropores, bubble OM pores, sponge-like pores, and cheese-like OM pores make a major contribution to shale pore space.

CRediT authorship contribution statement

Shasha Hui: Conceptualization, Methodology, Writing – original draft, Writing – review & editing, Funding acquisition. **Xiongqi Pang:** Investigation, Resources, Writing – review & editing, Funding acquisition. **Zhuoheng Chen:** Writing – review & editing, Supervision. **Tao Hu:** Investigation, Visualization, Supervision. **Kanyuan Shi:** Methodology, Software. **Guidong Di:** Investigation, Project administration. **Min Li:** Validation, Data curation. **Shuxing Mei:** Formal analysis. **Maowen Li:** Supervision.

Declaration of Competing Interest

The authors declare that they have no known competing financial interests or personal relationships that could have appeared to influence the work reported in this paper.

Data availability

Data will be made available on request.

Acknowledgments

The authors are indebted to the Joint Funds of the National Natural Science Foundation of China (U19B6003-02), the National Natural Science Foundation of China (42202133), the 2022 AAPG Foundation Grants-in-Aid Program (22269437), the Foundation of State Key Laboratory of Shale Oil and Gas Enrichment Mechanisms and Effective Development (33550000-21-ZC0613-0328), and SINOPEC Southwest Branch Company for financial support. Likewise, this study has benefited greatly from the anonymous reviewers for their professional and insightful comments.

References

Ardakani, O.H., Sanei, H., Ghanizadeh, A., Lavoie, D., Chen, Z., Clarkson, C.R., 2018. Do all fractions of organic matter contribute equally in shale porosity? A case study from Upper Ordovician Utica Shale, southern Quebec, Canada. Mar. Petrol. Geol. 92, 794–808.

Arif, M., Mahmoud, M., Zhang, Y., Iglauer, S., 2021. X-ray tomography imaging of shale microstructures: A review in the context of multiscale correlative imaging. Int. J. Coal Geol. 233, 103641.

Barrett, E.P., Johner, L.S., Halenda, P.P., 1951. The determination of pore volume and area distribution in porous substances. I. Computations from nitrogen isotherms. J. Am. Chem. Soc. 73, 373–380.

Berner, R.A., 1984. Sedimentary pyrite formation: an update. Geochim. Cosmochim. Acta 48 (4), 605–615.

Bousige, C., Ghimbeu, C.M., Vix-Guterl, M., Pomerantz, A.E., Suleimenova, A., Vaughan, G., Garbarino, G., Frygenson, M., Wildgruber, C., Ulm, F., Pellenq, R.J., Coasne, B., 2016. Realistic molecular model for kerogen's nanostructure. Nat. Mater. 15, 576–582.

Brunauer, S., Emmet, P.H., Teller, E., 1938. Adsorption of gases in multimolecular layers. J. Am. Chem. Soc. 60, 309–319.

Burst, J.F., 1969. Diagenesis of gulf coast clayey sediments and its possible relation to petroleum migration. AAPG Bull. 53 (1), 73–93.

Bustin, R.M., Bustin, A.M.M., Cui, X., Ross, D., Pathi, V.M., 2008. Impact of shale properties on pore structure and storage characteristics. Society of petroleum engineers, shale gas production conference in Fort Worth.

Cao, T., Song, Z., Wang, S., Cao, X., Li, Y., Xia, J., 2015. Characterizing the pore structure in the Silurian and Permian shales of the Sichuan Basin, China. Mar. Pet. Geol. 61, 140–150.

Cao, T., Deng, M., Cao, Q., Huang, Y., Yu, Y., Cao, X., 2021. Pore formation and evolution of organic-rich shale during the entire hydrocarbon generation process: Examination of artificially and naturally matured samples. J. Nat. Gas Sci. Eng. 93, 104020.

Cao, T., Liu, H., Pan, A., Fu, Y.u., Deng, M., Cao, Q., Huang, Y., Yu, Y., 2022. Pore evolution in siliceous shales and its influence on shale gas-bearing capacity in eastern Sichuan-western Hubei, China. J. Pet. Sci. Eng. 208, 109597.

Chandra, D., Vishal, V., 2021. A critical review on pore to continuum scale imaging techniques for enhanced shale gas recovery. Earth Sci. Rev. 217, 103638.

Chandra, D., Vishal, V., Debbarma, A., Banerjee, D.S., Pradhan, S.P., Mishra, M.K., 2020. Role of composition and depth on pore attributes of Barakar Formation gas shales of Ib Valley, India using a combination of low pressure sorption and image analysis. Energy Fuel 34, 8085–8098.

Chen, Y., Xu, J., Wang, P., 2020. Shale gas potential in China: A production forecast of the Wufeng-Longmaxi Formation and implications for future development. Energy Policy 147, 111868.

Chen, Y., Jiang, C., Leung, J.Y., Wojtanowicz, A.K., Zhang, D., 2021. Multiscale characterization of shale pore-fracture system: Geological controls on gas transport and pore size classification in shale reservoirs. J. Pet. Sci. Eng. 202, 108442.

Chen, Q., Zhang, J., Tang, X., Li, W., Li, Z., 2016. Relationship between pore type and pore size of marine shale: An example from the Sinian-Cambrian formation, upper Yangtze region, South China. Int. J. Coal Geol. 158, 13–28.

Chuhan, F.A., BjRlykke, K., Lowrey, C., 2000. The role of provenance in illitization of deeply buried reservoir sandstones from Haltenbanken and north Viking Graben, offshore Norway. Mar. Pet. Geol. 17 (6), 673–689.
Clarkson, C.R., Solano, N., Bustin, R.M., Bustin, A.M.M., Chalmers, G.R.L., He, L., Melnichenko, Y.B., Radliński, A.P., Blach, T.P., 2013. Pore structure characterization of North American shale gas reservoirs using USANS/SANS, gas adsorption, and mercury intrusion. Fuel 103, 606–616.
Comisky, J.T., Santiago, M., McColom, B., Budhala, A., Newsham, K.E., 2011. Sample size effects on the application of mercury injection capillary pressure for determining the storage capacity of tight gas and Oil shales: Canadian unconventional resources conference. https://doi.org/10.2118/149432-MS.
Dai, J., Zou, C., Liao, S., Dong, D., Ni, Y., Huang, J., Wu, W., Gong, D., Huang, S., Hu, G., 2014. Geochemistry of the extremely high thermal maturity Longmaxi shale gas, southern Sichuan Basin. Org Geochem. 74, 3–12.
Daniel, J.K.R., Marc, B., 2009. The importance of shale composition and pore structure upon gas storage potential of shale gas reservoirs. Mar. Pet. Geol. 26 (6), 916–927.
Furmann, A., Mastalerz, M., Schimmelmann, A., Pedersen, P.K., Bish, D., 2014. Relationships between porosity, organic matter, and mineral latter in mature organic-rich marine mudstones of the Belle Fourche and Second White Specks formations in Alberta, Canada. Mar. Pet. Geol. 54, 65–81.
Gao, Z.Y., Zhu, L., Hu, Q.H., Jiang, Z.X., Xuan, Q.X., 2021. A new and integrated imaging and compositional method to investigate the contributions of organic matter and inorganic minerals to the pore spaces of lacustrine shale in China. Mar. Pet. Geol. 127, 104962.
Guo, X., LI, Y., Borjigen, T., Wang, Q., Yuan, T., Shen, B., Ma, Z., Wei, W., 2020. Hydrocarbon generation and storage mechanisms of deep-water shelf shales of Ordovician Wufeng Formation–Silurian Longmaxi Formation in Sichuan Basin, China. Petroleum Exploration and Development 47, 204-213.
Han, H., Pang, P., Li, Z., Shi, P., Guo, C., Liu, Y., Chen, S., Lu, J., Gao, Y., 2019. Controls of organic and inorganic compositions on pore structure of lacustrine shales of Chang 7 member from Triassic Yanchang Formation in the Ordos Basin, China. Mar. Pet. Geol. 100, 270–284.
Ibad, S.M., Padmanabhan, E., 2022. Lithofacies, mineralogy, and pore types in Paleozoic gas shales from Western Peninsular Malaysia. J. Pet. Sci. Eng. 212.
Jarvie, D.M., Hill, R.J., Ruble, T.E., Pollastro, R.M., 2007. Unconventional shale-gas systems: The Mississippian Barnett Shale of north-central Texas as one model for thermogenic shale-gas assessment. AAPG Bull. 91, 475–499.
Jiang, Z., Tang, X., Li, Z., Huang, H., Yang, P., Yang, X., Li, W., Hao, J., 2016. The whole-aperture pore structure characteristics and its effect on gas content of the Longmaxi Formation shale in the southern Sichuan Basin. Earth Sci. Front. 23 (2), 126–134.
Jiang, Z., Song, Y., Tang, X., Li, Z., Wang, X., Guozhen, W., Xue, Z., Li, X., Zhang, K., Chang, J., Qiu, H., 2020. Controlling factors of marine shale gas differential enrichment in southern China. Pet. Explor. Dev. 47, 661–673.
Katsube, T. J., Issler, D.R., 1993. Pore-size distributions of shales from the Beaufort-Mackenzie Basin, northern Canada. Ottawa, Ontario. Geol. Surv. Cana. 93–1E, 123–132.
Ko, L.T., Ruppel, S.C., Loucks, R.G., Hackley, P.C., Zhang, T., Shao, D., 2018. Pore-types and pore-network evolution in Upper Devonian-Lower Mississippian Woodford and Mississippian Barnett mudstones: Insights from laboratory thermal maturation and organic petrology. International Journal of Coal Geology 190, 3-28.
Lazar, O.R., Bohacs, K.M., Macquaker, J.H.S., Schieber, J., Demko, T.M., 2015. Capturing key attributes of fine-grained sedimentary rocks in outcrops, cores, and thin sections: nomenclature and description guidelines. J. Sediment. Res. 85, 230–246.
Li, X., Jiang, Z.X., Wang, S., Wu, F., Miao, Y.A., Wang, X.M., Wang, H.X., Liu, X.B., 2022b. Differences of marine and transitional shales in the case of dominant pore types and exploration strategies, in China. J. Nat. Gas Sci. Eng. 103, 104628.
Li, M., Pang, X.Q., Luo, B., Wang, W., Cao, X.Y., Hu, T., Hui, S.S., Li, C.R., 2021b. Application of hydrocarbon generation potential method to deep shale gas resource evaluation: A case study of high-quality source rocks of the Wufeng-Longmaxi formation in the Sichuan Basin. J. China Univ. Min. Technol. 50, 1096–1107.
Li, M., Pang, X., Xiong, L., Hu, T., Chen, D., Zhao, Z., Hui, S., Liu, Y., Zhang, S., 2022a. The main controlling factors on shale gas occurrence characteristics in deep and high-over mature shales: A case study of Silurian Longmaxi Formation in the Sichuan Basin v. 8, 6901–6913.
Li, J.Z., Tao, X.W., Bai, B., Huang, S.P., Jiang, Q.C., Zhao, Z.Y., Cheng, Y.Y., Ma, D.B., Zhang, L.P., Li, N.X., Song, W., 2021a. Geological conditions, reservoir evolution and favorable exploration directions of marine ultra-deep oil and gas in China. Pet. Explor. Dev. 48, 52–67.
Li, J., Yin, J., Zhang, Y., Lu, S., Wang, W., Li, J., Chen, F., Meng, Y., 2015. A comparison of experimental methods for describing shale pore features-A case study in the Bohai Bay Basin of eastern China. Int. J. Coal Geol. 152, 39–49.
Liu, B., Mastalerz, M., Schieber, J., 2022. SEM petrography of dispersed organic matter in black shales: A review. Earth Sci. Rev. 224, 103874.
Liu, K., Ostadhassan, M., Gentzis, T., Fowler, H., 2019. Image analysis of the pore structures: An intensive study for Middle Bakken. J. Nat. Gas Sci. Eng. 61, 32–45.
Loucks, R.G., Reed, R.M., Ruppel, S.C., Jarvie, D.M., 2009. Morphology, Genesis, and Distribution of Nanometer-Scale Pores in Siliceous Mudstones of the Mississippian Barnett Shale. J. Sediment. Res. 79, 848–861.
Loucks, R.G., Reed, R.M., Ruppel, S.C., Hammes, U., 2012. Spectrum of pore types and networks in mudrocks and a descriptive classification for matrix-related mudrock pores. AAPG Bull. 96, 1071–1098.
Lowell, S., Shields, J.E., Thomas, M.A., Thommes, M., 2012. Characterization of Porous Solids and Powders: Surface Area, Pore Size and Density. Springer, Dordrecht, Netherlands, p. 16.
Luo, Q., Hao, J., Skovsted, C.B., Xu, Y., Liu, Y., Wu, J., Zhang, S., Wang, W., 2018. Optical characteristics of graptolite-bearing sediments and its implication for thermal maturity assessment. Int. J. Coal Geol. 195, 386–401.
Lyu, C., Zhang, Y., Li, C., Chen, G., Zhou, Q., Ma, M., Sun, Z., Gao, X., 2020. Pore characterization of Upper Ordovician Wufeng Formation and Lower Silurian Longmaxi Formation shale gas reservoirs, Sichuan Basin. China. J. Nat. Gas Geosci. 5 (6), 327–340.
Ma, Y.S., Cai, X.Y., Zhao, P.R., 2018. China's shale gas exploration and development: Understanding and practice. Pet. Explor. Dev. 45 (4), 561–574.
Ma, X.H., Xie, J., 2018. The progress and prospects of shale gas exploration and development in southern Sichuan Basin. SW China. Petroleum Exploration and Development 45 (1), 172–182.
Mastalerz, M., Schimmelmann, A., Drobniak, A., Chen, Y., 2013. Porosity of Devonian and Mississippian New Albany Shale across a maturation gradient: Insights from organic petrology, gas adsorption, and mercury intrusion. AAPG Bull. 97, 1621–1643.
Mathia, E.J., Bowen, L., Thomas, K.M., Aplin, A.C., 2016. Evolution of porosity and pore types in organic-rich, calcareous, Lower Toarcian Posidonia Shale. Mar. Pet. Geol. 75, 117–139.
Milliken, K.L., Rudnicki, M., Awwiller, D.N., Zhang, T., 2013. Organic matter-hosted pore system, Marcellus Formation (Devonian), Pennsylvania. AAPG Bull. 97, 177–200.
Milliken, K.L., Ko, L.T., Pommer, M., Marsaglia, K.M., 2014. Petrography of eastern Mediterranean Sapropels: analogue data for assessing organic matter in oil and gas shales. J. Sediment. Res. 84, 961–974.
Nelson, P.H., 2009. Pore-throat sizes in sandstones, tight sandstones, and shales. AAPG Bull. 93, 329–340.
Nie, R., Zhou, J., Chen, Z., Liu, J., Pan, Y., 2021. Pore structure characterization of tight sandstones via a novel integrated method: A case study of the Sulige gas field, Ordos Basin (Northern China). J. Asian Earth Sci. 213, 104739.
Peng, N., He, S., Hu, Q., Zhang, B., He, X., Zhai, G., He, C., Yang, R., 2019. Organic nanopore structure and fractal characteristics of Wufeng and lower member of Longmaxi shales in southeastern Sichuan, China. Mar. Petrol. Geol. 103, 456–472.
Peng, J., Milliken, K.L., Fu, Q., 2020a. Quartz types in the Upper Pennsylvanian organic-rich Cline Shale (Wolfcamp D), Midland Basin, Texas: Implications for silica diagenesis, porosity evolution and rock mechanical properties. Sedimentology 67, 2040–2064.
Peng, J., Milliken, K.L., Fu, Q., Janson, X., Hamlin, H.S., 2020b. Grain assemblages and diagenesis in organic-rich mudrocks, Upper Pennsylvanian Cline shale (Wolfcamp D), Midland Basin, Texas. AAPG Bull 104, 1593–1624.
Peng, S., Zhang, T., Loucks, R.G., Shultz, J., 2017. Application of mercury injection capillary pressure to mudrocks: Conformance and compression corrections. Mar. Pet. Geol. 88, 30–40.
Petersen, H.I., Schovsbo, N.H., Nielsen, A.T., 2013. Reflectance measurements of zooclasts and solid bitumen in Lower Paleozoic shales, southern Scandinavia: correlation to vitrinite reflectance. Int. J. Coal Geol. 114, 1–18.
Pommer, M., Milliken, K., 2015. Pore types and pore-size distributions across thermal maturity, Eagle Ford Formation, southern Texas. AAPG Bull. 99, 1713–1744.
Rigby, P.A., Dobos, S.K., Cook, F.J., Goonetilleke, A., 2006. Role of organic matter in framboidal pyrite oxidation. Sci. Total Environ. 367, 2–3.
Ross, D.J.K., Marc Bustin, R., 2009. The importance of shale composition and pore structure upon gas storage potential of shale gas reservoirs. Mar. Pet. Geol. 26, 916–927.
Schoenherr, J., Littke, R., Urai, J.L., Kukla, P.A., Rawahi, Z., 2007. Polyphase thermal evolution in the Infra-Cambrian Ara Group (South Oman Salt Basin) as deduced by maturity of solid reservoir bitumen. Org Geochem. 38, 1293–1318.
Shi, K., Pang, X., Chen, J., Hui, S., Yuan, W., Chen, J., Hu, T., Li, M., Zhang, K., Liu, Y., Zhang, S., You, T., 2023. Pore Structure Characteristics and Evaluation of Carbonate Reservoir: A Case Study of Lower Carboniferous in Marsel Exploration Area. Chu-Sarysu Basin. Nat. Resour. Res. 32, 771-793..
Slatt, R.M., O'Brien, N.R., 2011. Pore types in the Barnett and Woodford gas shales: Contribution to understanding gas storage and migration pathways in fine-grained rocks. AAPG Bull. 95, 2017–2030.
Sun, P., Xu, H., Zhu, H., Jia, L., Hu, X., Fang, H., Jiang, H., Xu, Z., Jiang, T., Jiang, X., Tian, L., 2021. Investigation of pore-type heterogeneity and its control on microscopic remaining oil distribution in deeply buried marine clastic reservoirs. Mar. Pet. Geol. 123, 104750.
Tang, X.L., Jiang, Z.X., Li, Z., Gao, Z.Y., Bai, Y.Q., Zhao, S., Feng, J., 2015. The effect of the variation in material composition on the heterogeneous pore structure of high-maturity shale of the Silurian Longmaxi formation in the southeastern Sichuan Basin, China. J. Nat. Gas Sci. Eng. 23, 464–473.
Tang, X.L., Jiang, Z.X., Jiang, S., Li, Z., 2016. Heterogeneous nanoporosity of the Silurian Longmaxi Formation shale gas reservoir in the Sichuan Basin using the QEMSCAN, FIB-SEM, and nano-CT methods. Mar. Pet. Geol. 78, 99–109.
Teng, J., Liu, B., Mastalerz, M., Schieber, J., 2022. Origin of organic matter and organic pores in the overmature Ordovician-Silurian Wufeng-Longmaxi Shale of the Sichuan Basin. China. International Journal of Coal Geology 253, 103970.
Tian, W.C., Lu, S.F., Huang, W.B., Wang, W.M., Li, J.J., Gao, Y., Zhan, Z.C., Sun, Y.F., 2020. Quantifying the control of pore types on fluid mobility in low-permeability conglomerates by integrating various experiments. Fuel 275, 117835.
Tian, H., Pan, L., Xiao, X.M., Ronald, W.T.W., Meng, Z.P., Huang, B.J., 2013. A preliminary study on the pore characterization of Lower Silurian black shales in the Chuandong Thrust Fold Belt, southwestern China using low pressure N2 adsorption and FE-SEM methods. Mar. Pet. Geol. 48, 8–19.

Voss, R.F., Laibowitz, R.B., Alessandrini, E.I., 1991. Fractal Geometry of Percolation in Thin Gold Films. Scaling Phenomena in Disordered Systems. Springer, US, pp. 279–288.
Wang, Y., 2017. Nanoscale pore structure evolution and shale gas occurrence of Longmaxi formation in upper Yangtze area. China University of mining & technology Beijing, p. 173.
Wang, E.Z., Guo, T.L., Li, M.W., Li, C.R., Dong, X.X., Zhang, N.X., Feng, Y., 2022b. Exploration potential of different lithofacies of deep marine shale gas systems: Insight into organic matter accumulation and pore formation mechanisms. J. Nat. Gas Sci. Eng. 102, 104563.
Wang, P., Jiang, Z., Ji, W., Zhang, C., Yuan, Y., Chen, L., Yin, L., 2016. Heterogeneity of intergranular, intraparticle and organic pores in Longmaxi shale in Sichuan Basin, South China: Evidence from SEM digital images and fractal and multifractal geometries. Mar. Pet. Geol. 72, 122–138.
Wang, E.Z., Feng, Y., Guo, T.L., Li, M.W., 2022a. Oil content and resource quality evaluation methods for lacustrine shale: A review and a novel three-dimensional quality evaluation model. Earth-Sci. Rev. 232, 104134.
Wang, X., Liu, L., Wang, Y., Sheng, Y., Zheng, S., Wu, W., Luo, Z., 2020. Comparison of the pore structures of Lower Silurian Longmaxi Formation shales with different lithofacies in the southern Sichuan Basin, China. J. Nat. Gas Sci. Eng. 81, 103419.
Washburn, E.W., 1921. Note on the method of determining the distribution of pore sizes in a porous material. Proceedings of the National Academy of Sciences of the United States of America 7, 115–116.
Wu, Z., He, S., Li, X., Liu, X., Zhai, G., Huang, Z., Yang, W., 2022. Comparative study on pore structure characteristics of marine and transitional facies shales: A case study of the Upper Permian Longtan Formation and Dalong Formation in the Lower Yangtze area, south China. J. Pet. Sci. Eng. 215, 110578.
Xu, S., Hao, F., Shu, Z., Zhang, A., Yang, F., 2020. Pore structures of different types of shales and shale gas exploration of the Ordovician Wufeng and Silurian Longmaxi successions in the eastern Sichuan Basin, South China. J. Asian Earth Sci. 193, 104271.
Xu, L., Yang, K., Wei, H., Liu, L., Li, X., Chen, L., Xu, T., Wang, X., 2021a. Pore evolution model and diagenetic evolution sequence of the Mesoproterozoic Xiamaling shale in Zhangjiakou, Hebei. J. Pet. Sci. Eng. 207, 109115.
Xu, L., Yang, K., Wei, H., Liu, L., Li, X., Chen, L., Xu, T., Wang, X., 2021b. Diagenetic evolution sequence and pore evolution model of Mesoproterozoic Xiamaling organic-rich shale in Zhangjiakou, Hebei, based on pyrolysis simulation experiments. Mar. Pet. Geol. 132, 105233.
Yang, F., Ning, Z., Liu, H., 2014. Fractal characteristics of shales from a shale gas reservoir in the Sichuan China. Fuel 115, 378–384.
Zhang, W.W., 2020. Pore and pressure evolution and of Longmaxi formation shale and transformation of shale gas occurrence in southern Sichuan. China University of Petroleum (Beijing), China, p. 137.
Zhang, Q., Liu, R.H., Pang, Z.L., Lin, W., Bai, W.H., Wang, H.Y., 2016. Characterization of microscopic pore structures in Lower Silurian black shale (S1l), southeastern Chongqing, China. Mar. Pet. Geol. 71, 250–259.
Zhao, J., Jin, Z., Jin, Z., Hu, Q., Hu, Z., Du, W., Yan, C., Geng, Y., 2017. Mineral types and organic matters of the Ordovician-Silurian Wufeng and Longmaxi Shale in the Sichuan Basin, China: Implications for pore systems, diagenetic pathways, and reservoir quality in fine-grained sedimentary rocks. Mar. Pet. Geol. 86, 655–674.
Zhao, W.Z., Li, J.Z., Yang, T., Wang, S.F., Huang, J.L., 2016. Geological difference and its significance of marine shale gases in South China. Pet. Explor. Dev. 43 (4), 547–559.
Zhao, R., Xue, H., Lu, S., Li, J., Tian, S., Wang, M., Dong, Z., 2022. Multi-scale pore structure characterization of lacustrine shale and its coupling relationship with material composition: An integrated study of multiple experiments. Mar. Pet. Geol. 140, 105648.
Zhong, X., Zhu, Y., Jiao, T., Qi, Z., Luo, J., Xie, Y., Liu, L., 2021. Microscopic pore throat structures and water flooding in heterogeneous low-permeability sandstone reservoirs: A case study of the Jurassic Yan'an Formation in the Huanjiang area, Ordos Basin, Northern China. J. Asian Earth Sci. 219, 104903.